NOVA SCHOOL OF SCIENCE & TECHNOLOGY

DEPARTMENT OF MATERIALS SCIENCE

PEDRO FERNANDO SANTOS SOUSA

Bachelor of Science in Micro and Nanotechnology Engineering

Hydrogen-doped Indium Oxide as transparent back contact for $Cu(In,Ga)Se_2$ thin film solar cells

MASTER OF SCIENCE IN MICRO AND NANOTECHNOLOGY ENGINEERING

NOVA University Lisbon

October, 2022

DEPARTMENT OF MATERIALS SCIENCE

Hydrogen-doped Indium Oxide as transparent back contact for $Cu(In,Ga)Se_2$ thin film solar cells

PEDRO FERNANDO SANTOS SOUSA

Bachelor of Science in Micro and Nanotechnology Engineering

Adviser: Dr. Sascha Sadewasser
Principal Investigator – Laboratory for Nanostructured Solar Cells, International Iberian Nanotechnology Laboratory

Co-adviser: Dr. Manuel Mendes,
Assistant Professor, NOVA School of Science and Technology

Examination Committee:

Chair: Dr. Hugo Águas,
Full Professor, *NOVA School of Science and Technology*

Rapporteur: Dr. Paulo Fernandes,
Assistant Professor, *Instituto Superior de Engenharia do Porto*

Adviser: Dr. Sascha Sadewasser,
Principal Investigator – Laboratory for Nanostructured Solar Cells, *International Iberian Nanotechnology Laboratory*

Co-adviser: Dr. Manuel Mendes,
Assistant Professor, *NOVA School of Science and Technology*

MASTER OF SCIENCE IN MICRO AND NANOTECHNOLOGY ENGINEERING

NOVA University Lisbon
October 2022

Hydrogen-doped Indium Oxide as transparent back contact for Cu(In,Ga)Se_2 thin film solar cells

ACKNOWLEDGMENTS

This thesis is the closing chapter of my past 6 years as a university student, which would have not been possible without the support of colleagues, friends, and family.

Firstly, I would like to acknowledge Prof. Dr. Rodrigo Martins, Prof. Drª. Elvira Fortunato and all the Material's Science Department for providing us students with the best learning and working conditions at the university.

I would like to thank my supervisor, Dr. Sascha Sadewasser, for accepting me as a member of the LaNaSC group at INL and for all the support and experienced insight. To my FCT-UNL co-supervisor, Dr. Manuel Mendes, for being always available to help and for all the academic support throughout these 6 years of learning.

Despite paper formalities, I would like to thank my practical supervisor in INL, Ph.D. student Marina Alves, for all the time, patience, and tolerance you have demonstrated during this project. For teaching me on lab work and most of all for being an amazing friend, thank you!

To the LaNaSC former and current members, Nicoleta, Anacleto, Elmahdi, Daniel, Francisco, Diego, Alessandro and Matej, thank you for the laidback lunch times and mostly entertaining talks. Santos, Kate, Maria, Patrícia, Wesley, Christian and Diana, the best interns LaNaSC will ever have, thank you for providing me with the best 6 months of this journey. Personally, I could not have asked for a better team to support me during this time. Thank you for all the hard laughs, night outs at Rick's, field trips and specially for being genuine and truly good friends. I will be visiting soon!

To a very special person, Diana, I cannot thank you enough. Through the good and bad we have been there for each other. Your generosity and kindness brought me many joys. Thank you for all you have taught me, for trusting me and for always being cheerful and positive. I owe you a lot.

For what has been my second home for 6 months, I must thank everyone in Rua Bairro Henriqueta nº 15. André, Gui, Edu, Xico and Jeff you were the best housemates I have had. Afternoons filled with music, long talks about politics and for sharing the love for F1 and FOX Comedy. Thank you.

To my university friends, you will stay with me forever. We have gone through many hardships together, but we still endured. From all the parties and sleep overs to endless nights trying to survive uni courses, you have been present in every single aspect of my academic life. Though some distance may do us apart, I know that we can count on each other.

To my friends in Madeira, I have known you for a long time. Few words are needed between us, but I cannot thank you enough. You mean the world to me.

To my family, mother, father and brother, your unconditional love and support kept me going through these past months. You show me that hard work and dedication pays off and in the end what you can learn from the experience, whether successful or not, is what really counts. I love you and I dedicate this to you!

“The only real mistake is the one from which we learn nothing.”
Henry Ford

ABSTRACT

Due to its high mobility and transparency, hydrogen-doped indium oxide films, In_2O_3:H (IOH), films can be used as a transparent back contact (TBC) for Cu(In,Ga)Se_2 (CIGSe) thin film solar cells in semi-transparent applications, such as bifacial or tandem solar cells. To serve as a back contact, the IOH films must create an ohmic contact with the absorber layer, be highly transparent and have low sheet resistance (R_{SH}). In this study, a process optimization of amorphous IOH deposition by radio-frequency (RF) magnetron sputtering, with no intentional heating, was performed. Parameters such as hydrogen content and power density were varied to obtain the desired optoelectronic properties. A post-deposition annealing was performed, under high vacuum conditions (1-5×10^{-7} mbar), to crystallize the amorphous phase. The optoelectronic properties of the IOH films were characterized by 4-point probe for the sheet resistance, UV-VIS-NIR spectrophotometer for transmittance and X-ray diffraction (XRD) for the structural properties. An optimized 500 nm thick IOH film with R_{SH}=7.26±0.140 Ω/sq and average visible transmittance (AVT) of 81 % was produced and used as a transparent back contact for a CIGSe solar cell.

Keywords: Semi-transparent films; In_2O_3:H; radio-frequency magnetron sputtering; Cu(In,Ga)Se_2

RESUMO

Devido à sua alta mobilidade e transparência, filmes de óxido de índio dopado com hidrogénio, In2O3:H (IOH), podem ser usados como um contacto transparente em células solares de filme fino como Cu(In,Ga)Se2 (CIGSe), para aplicações semitransparentes, como células solares bifaciais ou tandem. Para servir como contacto transparente, os filmes de IOH têm de criar um contacto óhmico juntamente com a camada absorvente, ser altamente transparentes e apresentar um baixo valor de resistência folha (R_{SH}). Neste estudo, foi feito um processo de otimização de deposição de filmes amorfos de IOH por pulverização catódica de radiofrequência com magnetrão, sem aquecimento intencional. Parâmetros como o conteúdo de hidrogénio e energia fornecida foram variados de forma a obter as características optoelectrónicas desejadas. Um recozimento pós-deposição foi utilizado, sobre condições de pressão em alto vácuo ($1\text{-}5\times10^{-7}$ mbar) para cristalizar a fase amorfa dos filmes. As propriedades optoelectrónicas dos filmes de IOH foram caracterizadas por método das quatro pontas para a resistência folha, espetrofotómetro UV-VIS-IV para a transmitância e difração de raios X para as propriedades estruturais. Um filme de IOH otimizado com 500 nm de espessura, uma R_{SH}=7.26±0.140 Ω/sq e uma transmitância visível média de 81 % foi produzido e utilizado como contacto transparente numa célula solar de CIGSe.

Palavras chave: Filmes semitransparentes; In_2O_3:H; pulverização catódica de radiofrequência com magnetrão; $Cu(In,Ga)Se_2$

CONTENTS

LIST OF FIGURES

LIST OF TABLES

ACRONYMS

Acronym	Name
4PP	4-point probe
AVT	Average visual transmittance
AZO	Aluminum doped zinc oxide
CBD	Chemical bath deposition
CGI	[Cu]/([Ga]+[In])
CGS	Copper gallium selenide
CIG	Copper indium gallium
CIGSe	Copper indium gallium diselenide
CVD	Chemical vapor deposition
DC	Direct Current
DIW	Deionized water
EDX	Energy dispersive X-Ray Spetroscopy
FTO	Fluorine doped tin oxide
GGI	[Ga]/([Ga]+[In])
INL	International iberian nanotechnology laboratory
IO	Indium oxide
IOH	Hydrogen doped indium oxide
ITO	Tin doped indium oxide
I-V	Current-voltage
J-V	Current Density-voltage
KPFM	Kelvin-probe force microscopy
NIR	Near infrared
PCE	Power conversion eficciency
PDT	Post deposition treatment
PV	Photovoltaics

RF	Radio frequency
SEM	Scanning electron microscopy
SLG	Soda lime glass
SPC	Solid phase crystallization
STAR	Sputtering for advanced research
TBC	Transparent back contact
TCO	Transparent conductive oxide
TEM	Transmission electron microscopy
UV	Ultra-violet
VIS	Visible
XPS	X-ray photoelectron spectroscopy
XRD	X-ray diffraction

SYMBOLS

Symbol	Name	Unit
Al	Aluminum	
Al_2O_3	Aluminum oxide	
Ar	Argon	
a-si	Amorphous silicon	
Au	Gold	
Cd	Cadmium	
CdS	Cadmium sulfide	
CdTe	Cadmium telluride	
Cr	Chromium	
c-Si	Crystalline silicon	
$Cu(In,Ga)Se_2$	Copper indium gallium diselenide	
$Cu_{2-x}Se$	Copper selenide	
E_f	Formation energy	eV
E_g	Bandgap	eV
E_g^{bottom}	Bandgap bottom cell	eV
E_g^{top}	Bandgap top cell	eV
FF	Fill factor	%
Ga_2O_3	Gallium oxide	

GaAs	Gallium arsenide	
H_2O	Water	
In_2O_3:H	Hydrogen doped indium oxide	
In_2O_3:Sn	Tin doped indium oxide	
I_{SC}	Short-circuit current	A
i-ZnO	Intrinsic zinc oxide	
J_{SC}	Short circuit current density	mA/cm2
KCN	Potassium cyanide	
Mo	Molybdenum	
$MoSe_2$	Molybdenum diselenide	
N_2	Nitrogen	
Na	Sodium	
NaF	Sodium fluoride	
NH_4OH	Ammonium hydroxide	
Ni	Nickel	
PCE	Power conversion efficiency	%
$P_{density}$	Power density	W/cm2
P_{max}	Maximum power	W
R_s	Series resistance	Ω
R_{SH}	Sheet resistance	Ω/sq
R_{shunt}	Shunt resistance	Ω
Se	Selenium	
Si	Silicon	
SiO_2	Silicon dioxide	
SnO_2:F	Fluorine doped tin oxide	

Ti	Titanium	
V_{Cu}	Copper vacancy	
V_O^{++}	Oxygen vacancy	
V_{oc}	Open circuit voltage	V
W	Tungsten	
ZnMgO	Zinc magnesium oxide	
ZnO	Zinc oxide	
ZnO:Al	Aluminum doped zinc oxide	

1

INTRODUCTION

1.1 Motivation

Due to a rapid growth of the world's population and industrialization, greenhouse gas emissions and fossil fuel consumption have increased in the past decades. Problems such as global warming and non-renewable resources scarcity demands new, clean, and sustainable types of energy, ultimately searching for a replacement for fossil fuels [1]. Solar energy is the most abundant, thus promising form of renewable energy, having received significant attention in the scientific community over the past decades. Within solar energy applications lies photovoltaic technology, which converts sunlight into electricity using the photovoltaic effect. The photovoltaic effect consists of the absorption of incident photons, by a semiconductor material, to create electron-hole pairs. These pairs are separated by a *p-n* junction, thereby generating a potential difference. Connecting the solar cell to an external circuit allows electrons and holes to create a current [2].

The first generation of solar cells consists of crystalline silicon (c-Si) as absorber material. These solar cells represent around 95 % of the current PV market, can achieve high efficiencies (record efficiency of 26.7 %) [3] and have good reliability and stability. However, the use of Si-based cells has an economical drawback since the demand for high amounts of this material has risen along with its manufacturing cost. An alternative to these first-generation cells are the thin film solar cells such as amorphous silicon (a-Si), $Cu(In,Ga)Se_2$ (CIGSe) and cadmium telluride (CdTe), specified as second-generation solar cells. While silicon-wafer cells have absorber layers of 350 μm thickness, these thin films solar cells have absorber layers of about 1-5 μm, providing for most of the visible radiation to be absorbed and thus considerably reducing the quantity of semiconductor material used. Additionally, alternative deposition methods can reduce production costs [4], [5].

The third generation of solar cells aims to achieve high efficiency by overcoming the Shockley-Queisser limit for single bandgap devices [6] with systems of concentrators, organic solar cells like dye-sensitized solar cells and the multi-layered tandem cells made of a-Si, gallium arsenide (GaAs), perovskites and CIGSe [7]. The efficiency limit for single-junction solar cells is related with the absorber layer bandgap, which limits the open-circuit voltage (V_{OC}) as higher energy photons suffer from thermalization losses. A tandem architecture mitigates these losses by stacking two cells with different bandgaps: a top cell absorber layer with a higher bandgap (E_g^{top}) and a bottom cell absorber layer with a lower bandgap (E_g^{bottom}). This type of structure enables an efficient use of the solar spectrum with higher energy photons ($h\nu > E_g^{top}$) being absorbed by the top cell and lower energy photons ($h\nu < E_g^{top}$) being transmitted to the bottom cell, which will ultimately be absorbed by the lower E_g in the bottom cell absorber ($h\nu > E_g^{bottom}$) [8]. Optimum values for the two bandgaps ($E_g^{top} \approx 1.80$ eV, $E_g^{bottom} \approx 1.0$ eV) are required to maximize the power conversion efficiency (PCE) [9], [10], which makes absorber materials with tunable E_g, like CIGSe, a suitable candidate for these applications. CIGSe has a good absorption coefficient ($10^5\,cm^{-1}$), tunable bandgap (1.04 – 1.68 eV) and long term stability [11]. However, CIGSe solar cells commonly use an opaque molybdenum (Mo) back contact, thus impeding their

use as top cell in a tandem structure. It is proposed to use transparent conductive oxides (TCO) like hydrogen-doped indium oxide (In_2O_3:H) (IOH) to serve as a transparent back contact (TBC) to replace Mo. A successful implementation of a TBC on CIGSe solar cells can provide a good top subcell for tandem cells which require a TBC to transmit the incident light to the bottom subcell. Also, a TBC enables the CIGSe cell to be used as bifacial devices. Keller et al. presented a functioning bifacial CIGSe solar cell using IOH as a back contact with a PCE of 11.0 % at front side illumination and 6.0 % at back side illumination [12]. More on the reasoning behind this proposal will be discussed in section (1.3).

1.2 CIGSe technology and structure

Copper indium gallium diselenide-based solar cells represents the highest-efficiency alternative to large-scale, commercial Si photovoltaics, due to the direct bandgap of the absorber and low material consumption. They achieve high light to power conversion efficiencies, with a record of 23.35 % [13]. CIGSe solar cells consist of a stack of several layers, which will be introduced in the following.

Substrate

Most CIGSe solar cells are fabricated using the substrate configuration, where different layers are deposited on top of a substrate, usually soda lime glass (SLG) and the cell is irradiated from the top contact, the window layer. SLG has a similar thermal expansion coefficient to CIGSe, allowing process temperatures up to 530 ºC [14]. Besides its structural function, SLG acts as a sodium (Na) source for the absorber layer, which has shown to be a key factor for the improvement of the open-circuit voltage (V_{OC}) and fill factor (*FF*) values of CIGSe solar cells [15]. However, an uncontrolled diffusion of Na from the SLG during absorber deposition impedes the interdiffusion of the chemical elements, inducing detrimental gallium gradients. A post-deposition treatment (PDT) using sodium-fluoride (NaF) is a controlled process that induces the necessary Na amount for high efficiency CIGSe solar cells while avoiding pronounced Ga gradients [74].

Back contact

Molybdenum (Mo) is the preferred material to use as a back contact in CIGSe solar cells, due to its chemical and mechanical stability during absorber growth. Usually grown via sputtering, Mo shows high conductivity, strong adhesion, good Na permeability and establishes an ohmic contact with the absorber layer by forming an interfacial layer of $MoSe_2$ [16]. Nevertheless, different materials have been used as back contacts for different applications. Matson et al. [17] reported the use of metal contacts and determined that only gold (Au) and nickel (Ni) established an ohmic contact with the absorber. Orgassa et al. [18] fabricated CIGSe solar cells with other materials like tungsten (W), chromium (Cr) and titanium (Ti), and found that W and Mo contacts provide the best CIGSe/back contact interface passivation. For applications that require a transparent back contact, materials such as tin-doped indium oxide, (In_2O_3:Sn) (ITO), fluorine-doped tin oxide, SnO_2:F (FTO) [19] and IOH [12], [20], [21] were used instead of Mo.

Absorber layer

The absorber layer is the most important component of a solar cell as it is responsible for absorbing the incident radiation creating excess charge carriers, which will generate photocurrent. CIGSe is a *p*-type absorber that crystallizes in the tetragonal chalcopyrite structure. This material has raised a lot of attention due to its high absorption coefficient (10^5 cm^{-1}), good stability and direct bandgap, making it suitable for thin film applications since the layer only requires a thickness of 1-2 µm to absorb a

large fraction of the incident light, thus using less material [22], [23]. Its good conductivity results from intrinsic defects in the material due to shallow defect Cu vacancies (V_{Cu}) [24]. The vacancies act as an acceptor, thus holes are the majority charge carriers. Controlling the elemental composition of CIGSe is necessary to obtain a good quality absorber. The [Cu]/([Ga]+[In]) ratio (CGI) influences the grain growth of CIGSe films and the [Ga]/([Ga]+[In]) ratio (GGI) tunes the bandgap between 1.04 eV (GGI = 0) and 1.68 eV (GGI = 1)[25]. For high efficiency CIGSe solar cells, Nakamura et al. [13] states a CGI and GGI composition of 0.93 and 0.30, respectively, which goes in accordance with many other reports [26], [27]. Promoting a Cu-poor composition is essential for a relatively large phase stable region of the chalcopyrite and avoiding the formation of $Cu_{2-x}Se$ phases, which are detrimental to material and cell performance due to its semi-metallic nature, acting as an electron-hole recombination center and increasing conductivity creating an electric shunt [28].

Buffer layer

The buffer layer separates the absorber layer and the window layer, playing an important role in the interface formation. This layer protects the absorber layer from damage during window deposition, and since it is usually high-resistive, can prevent shunting between the front contact and the absorber [29]. Cadmium sulfide (CdS) has long been used to fabricate solar cells with an early appearance as a thick window layer [30]. The implementation of this material in CIGSe solar cells came later in 1987, serving as a buffer layer, grown via chemical bath deposition (CBD), leading then to an overall efficiency of 12 % [31]. CdS is a n-type semiconductor that forms the pn-heterojunction of the solar cell with the absorber. With a large bandgap of 2.4 eV [32] it absorbs high energy photons and lets the lower energy photons through to the absorber. This poses as a disadvantage since the CdS retains the photogenerated carriers (from high energy photons) in the layer thus not contributing to the photocurrent generated by the cell. CdS also grants for a good band alignment with CIGSe, maximizing the collection of photogenerated carriers [33]. Although CdS is a good candidate for great cell efficiencies, it is a toxic and carcinogenic material, making it non desirable. Alternatives are being studied, highlighting the record efficiency Cd-free cell of 23.35 % [13] using a $Zn(O,S,OH)_x$ film.

Window layer

The window layer is the top contact for the CIGSe solar cell. It requires high transmittance with low reflectivity, good conductivity, and minimal resistance. Zinc oxide (ZnO) is widely used as a material for window layers. It has a direct bandgap of 3.3 eV [34] and it is a low-cost, abundant, non-toxic material [35], [36] with a transparency over the visible spectrum and near infrared (NIR) range [37]. Researchers have also investigated intentionally doped materials like aluminum-doped zinc oxide ZnO:Al (AZO) [38], ITO [19], FTO [11] and IOH [39]–[41] to serve as window layers due to their stability and controllability. A typical CIGSe front contact consists of two radio frequency sputtered layers, an intrinsic zinc oxide (i-ZnO) which prevents short circuits and Al diffusion to the subsequent layers and a ZnO:Al layer that confers conductivity, transparency and is the front contact of the solar cell.

The full stack of a CIGSe solar cell with all its layers is presented in **Figure. 1.1**.

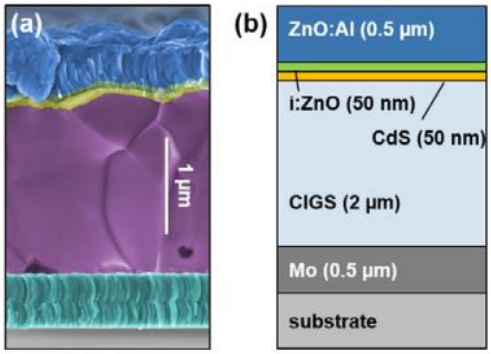

***Figure 1.1**- (a) Colored SEM cross section of a CIGSe sample. (b) Substrate configuration of a standard CIGSe solar cell.*[42]

1.3 IOH as a transparent back contact for CIGSe solar cells

Transparent conductive oxides (TCO) have been researched as highly transparent and conductive electrodes for optoelectronic applications, like solar cells, These inherent characteristics allow for low resistances without compromising light transmission or absorption. TCO are usually *n*-type materials i.e., electrons are the majority carriers. To achieve high values of conductivity, these films need to be degenerately doped. Intrinsic structural defects or extrinsic doping confers structural imperfections, which are crucial for understanding the mechanisms for good conductivity. In_2O_3 (IO) is a well-documented binary compound that crystallizes according to a cubic structure of the bixbyite mineral and exhibits a wide bandgap of 3.5-3.7 eV for light absorbed by direct interband transitions [43]. Its widespread application consists of the TCO ITO, which has found its main applications in liquid crystal displays, smart windows [44], [45] and as a transparent electrode in solar cells [46]. Likewise, another extrinsically doped TCO, FTO, found its use in solar cells applications [47]. FTO has a good visible transparency and low resistivity due to high carrier concentration caused by oxygen vacancies and substitutional fluorine [48].

This work focuses on IO doped with hydrogen (H_2) to serve as a transparent back contact (TBC) for thin film CIGSe solar cells. To pose as a TBC, the layer must establish an ohmic contact with the absorber, be highly transparent, exhibit a low sheet resistance (R_{SH}) and have mechanical and thermal stability upon absorber depostion [21]. A standard CIGSe solar cell uses Mo as a back contact (see section 1.1.2), leading to opaque devices. ITO and FTO have been researched and used as TBC in CIGSe solar cells, but both lacked efficacy when compared to Mo. Several performance losses were described [21], as the absorber deposition ($T > 500$ ºC) creates unfavorable conditions for the TCO. Using ITO, the formation of a highly resistive gallium oxide (Ga_2O_3) layer may create a reverse junction at the back contact/absorber interface, deteriorating especially the fill factor (*FF*) of the devices. On the other hand, FTO shows reduced conductivity when fluorine is lost. A solution passes through low temperature depositions for the CIGSe. However, high temperature depositions ($T \geq 500$ ºC) are recommended to improve grain growth and absorber quality [21].

IOH has a been thoroughly investigated by Koida et al. as a high-mobility (130 $cm^2/(V\ s)$) window layer [39]–[41] and as a back contact in CIGSe solar cells by Keller et al. [12], [20], [49] with a reported efficiency of 16.1 % for a (Ag,Cu)(In,Ga)Se_2 solar cell [21]. IOH is transparent, has high conductivity, small dispersion of refractive index and very low extinction coefficient in the visible to the near infra-

red (NIR) wavelengths [41]. Furthermore, it is possible to fabricate IOH films at relatively low temperatures (~200 ºC) using a solid phase crystallization step after room temperature sputtering of the amorphous films, with water (H_2O) addition in the sputtering gas [50]. H_2O doping has been thoroughly used in the fabrication of high mobility IOH films. However, very low concentrations of this dopant are necessary to obtain the desired properties, which poses to be a challenge when managing low gas flow in vacuum systems. Upon this drawback, researchers started using hydrogen (H) as a source of doping to simplify the deposition process [51], [52]. During the sputtering process, H is said to form a shallow donor state in metal oxides when incorporated at interstitial or substitutional sites. Structural rearrangements during the solid phase crystallization process eliminate oxygen deficiencies, generating H^+ (singly charged donors), substituting a doubly charged impurity, oxygen vacancy (V_O^{++}), for a singly charged one, reducing the carrier density and improving the film's mobility [39], [50]. It also plays an important role in enhancing the grain size and mitigating subgap defects in post-annealed IOH films, as its presence at the grain boundaries is considered to passivate defects to reduce transport barriers [51], [53].

1.4 Magnetron Sputtering

Magnetron sputtering is a high-vacuum physical vapor deposition (PVD) technique, where magnetic fields are used to trap electrons in the vicinity of a cathode target. Besides its uniform deposition rate over large areas and low-cost, this technique allows for high purity coatings depositions of different materials (metals, alloys, compound materials, dielectrics). A gas inlet supplies the process chamber with inert gases, usually Argon (Ar), and/or reactive gases to generate a plasma. A plasma is a partially ionized gas that contains accelerated cations and electrons. While trapped in a magnetic field, an electron can collide with an Ar atom, generating an Ar^+ ion. This ion will accelerate towards the cathode with enough energy to knock out some of the target's material, making these particles travel through the vacuum and depositing onto the substrate [54].

Direct current (DC) magnetron sputtering is widely accepted as an effective low-cost thin film deposition technique for electrically conductive target materials. DC magnetron sputtering has high deposition rates thus suitable for depositing large quantities of surface material onto substrates. However, this technique does not allow for insulator materials (e.g., oxides films) to be deposited. Moreover, DC sputtering creates unwanted charge build-up which hinders the quality control of the sputtered films.

Radio frequency (RF) magnetron sputtering is a variation of sputtering where a RF potential is used to prevent a charge accumulation on the target materials. By alternating the potential, simultaneous bombardment with both positive and negative ions occurs. Due to higher mobility than ions, electrons will reach the target's surface faster (in the positive cycle) than the positive ions (in the negative cycle), thus the target becomes negatively self-biased, warding off electrons near the target and giving room to the positive ions (Ar^+) to freely bombard the material and keep the sputtering process without any decay in performance. RF magnetron sputtering allows non-conducting insulating materials (e.g., aluminum oxide (Al_2O_3), silicon oxide (SiO_2), and others) to be deposited at good deposition rates (DC still yields a better deposition rate than RF [55]) and it also reduces arcing and racetrack erosion.

Reactive RF magnetron sputtering consists of depositing compound materials from a ceramic target in the presence of a reactive gas (e.g., O_2, N_2, CH_4) mixed with an inert gas, e.g., Ar.

2

MATERIALS AND METHODS

This section aims to demonstrate the process used throughout the project starting with a brief description on how substrates were prepared (2.1). Furthermore, insight on the process used to deposit IOH films (2.2) and a functioning CIGSe solar cell is described (2.3), followed by the characterization techniques utilized (2.4).

2.1 Substrate cleaning

Prior to the deposition of IOH films, the substrate must be cleaned using a multi-step ultrasound bath process. The SLG substrate, was placed in a substrate holder and into a beaker with an appropriate detergent – Fisherbrand™ MicroSon - and deionized water (DIW). The first bath is done with water at room temperature and soap for 10 minutes, followed by a second bath with water at 60 ºC for another 10 minutes. After these two steps, the substrates undergo 4-6 more DIW baths at 60 °C, 10 minutes each, until there is no soap left in the bath water. Once the cleaning is finished, each substrate was blow dried with a N_2 gun. In some cases, the clean substrates were patterned using a waterproof ink marker to allow quantification of film thickness, using contact profilometer, before loading them into the sputtering system.

2.2 In_2O_3:H deposition

All the sputtering depositions were performed on an *in*-situ fabrication system, called **S**pu**T**tering for **A**dvanced **R**esearch (STAR) [56], which is located at the Internationa Iberian Nanotechnology Laboratory (INL). IOH films, were fabricated by a two-step process: (i) growth of an amorphous layer by reactive RF magnetron sputtering, without intentional heating, and (ii) solid phase crystallization (SPC) in vacuum at 200 ºC for 1 hour. Two optimization series were performed to study the influence of the sputtering power and H_2 flux variations on the IOH films optoelectronic and structural properties. Three samples were deposited for each series: using a sputtering power variation between 2.0 and 3.0 W/cm^2 and a H_2 flux variation between 1.0 and 1.4 sccm. O_2 pulses were introduced into the chamber [using a MKS Instruments mass flow controller (100 sccm)] and a gas mixture of Ar/H_2 (5 % of H_2) was used to achieve hydrogen doping.

The IOH films were RF-sputtered from a compound In_2O_3 target with a 2-inch diameter at working pressures of 5.5-5.7×10^{-3} mbar. Ar and O_2 fluxes were set to 30 and 1.5 sccm, respectively while Ar/H_2 fluxes were varied as described above. O_2 pulses were set for a 3-minute loop: 1 minute with oxygen and 2 minutes without oxygen.

2.3 Solar cell fabrication

To test the IOH as a back contact for CIGSe solar cells, a complete solar cell device was fabricated at INL, with IOH back contact and Mo back contact as a reference. The solar cell structure consists of a stack of SLG/back contact (IOH or Mo)/CIGSe/CdS/ZnMgO/ZnO:Al.

The IOH back contact was RF-sputtered as described above, at a working pressure of 5.5-5.7× 10^{-3} mbar and power density ($P_{density}$) 2.5 W/cm^2. Ar, O_2 and Ar/H_2 fluxes were set to 30, 1.5 and 1.2 sccm, respectively, using O_2 pulses as described above. To obtain a 500 nm thick film, the process time was 120 minutes.

A standard Mo film was deposited by DC magnetron sputtering, using a two-step process to obtain a bi-layer molybdenum film. A 100 nm thick layer of Mo is sputtered at high pressure to ensure an adhesive film, followed by a 400 nm thick layer sputtered at lower pressure to confer low resistivity to the Mo back contact [57].

For the CIGSe absorber layer, a two-stage process is performed. First, a deposition of CuInGa (CIG) by co-sputtering of two CIG targets with composition of (50:35:15 at%) and (15:60:25 at%) is carried out without intentional substrate heating (see **Table 2.1** for deposition parameters). Then, to form the CIGSe compound, a post-annealing step in a selenium atmosphere (selenization) is performed in a tube furnace. The sample, together with some Se pellets (~100 mg), are placed inside a graphite box that goes into the tube furnace. Secondly, the tube is purged by performing a series of pumping and flushing with N_2 and Ar. Once the chamber is free from any contaminants, an Ar flux is set to 100 sccm and a heating ramp (25 ºC/minute until 100 ºC) is performed. After 30 min at 100 ºC, another heating ramp (25 ºC/ minute from 100 to 500 ºC) is done where the sample is held for 30 min. To cool down the sample, the power is turned off. After the temperature in the furnace reaches 400 ºC, the lid is opened, and the sample is unloaded at 60 ºC.

Table 2.1 - Absorber layer deposition parameters.

Target (at%)	Voltage (V)	Current (mA)	Ar flux (sccm)	Pressure (mbar)	Duration (min)
50:35:15	418	63	25	5.5×10^{-3}	72
15:60:25	458	12			

Before CdS deposition, a KCN-etching treatment (5% wt solution of KCN) of the absorber layer for 30 s is conducted to chemically etch any potential copper selenide ($Cu_{2-x}Se$). The CdS buffer layer is fabricated via CBD, using a solution that contains 1.33 g of thiourea, 0.13 g of cadmium acetate, 15 ml of ammonium hydroxide (NH_4OH) and 85 ml of DIW. To complete the solar cell, a transparent conductive oxide window layer consisting of 50 nm of a resistive layer, in this case ZnMgO, and 200 nm of ZnO:Al is deposited via RF magnetron sputtering. **Table 2.2** summarizes the process parameters used for both depositions.

Table 2.2 - Window layer deposition process parameters.

Layer	Thickness (nm)	Ar flux (sccm)	Pressure (mbar)	Power (W)	Duration (min)
ZnMgO	50	30	6.2×10^{-3}	50	14
ZnO:Al	200	35	5.5×10^{-3}	60	40

2.4 Characterization techniques

For the optimization of the IOH films, sheet resistance (R_{SH}) and thickness measurements were conducted, using a four-point probe (4PP) system (CMT-SR2000NW by AITCO) and contact profilometer (KLA-Tencor P-16) (step between the patterned SLG and IOH film), respectively. The optical transmission of the films was determined by using a Perkin Elmer Lambda 950 UV-VIS-NIR spectrophotometer with an integrating sphere. Structural changes of the IOH films and in the CIGSe solar cell were evaluated by X-ray diffraction (XRD) with a Panalytical X'Pert Pro MRD system using a Cu K_α as radiation source ($\lambda = 0.154$ nm). The morphology and composition of the produced CIGSe solar cells were determined using scanning electron microscopy (SEM) (FEI Quanta 650 FEG) and energy dispersive X-ray spectroscopy (EDX). To evaluate the performance of the solar cell, current-voltage (*J-V*) measurements were carried out.

3

RESULTS AND DISCUSSION

In this chapter, the results are presented and discussed in sections concerning: IOH films deposition process optimization (3.1) and the preparation of CIGSe solar cells using IOH as a back contact vs the reference cell with the standard Mo back contact (3.2).

3.1 IOH deposition process optimization

The optimization of the deposition process for IOH started from a previously developed process at an RF power of 30 W ($P_{density}$ = 1.5 W/cm^2) and working pressure of 5.5-5.7×10^{-3} mbar. The amorphous IOH film (as-deposited) exhibited R_{SH} 18±0.2 Ω/sq and average visual transmittance (AVT) of 86 %. Upon annealing, the R_{SH} went up to 28±0.1 Ω/sq and the AVT improved to 89 %.

3.1.1 Power variation series

For the first optimization series, the power density was varied with gases' flux rates fixed and the same O_2 pulses (1'ON+2'OFF) throughout the depositions. Three experimental runs (A, B and C) were performed using different power values: 40, 50 and 60 W corresponding to 2, 2.5 and 3 W/cm^2, respectively. After deposition, the films are subject to a solid-phase crystallization step by heating the substrate to 200 ºC for 1 hour, under high-vacuum conditions (1-5×10^{-7} mbar). The deposition time was adjusted, to maintain the thickness of the samples as constant as possible. **Table 3.1** shows the deposition parameters for these experiments.

Table 3.1 - Deposition parameters for the power variation series.

Sample	Process gases' flux (sccm)			Power Density (W/cm^2)	Deposition Time (min)	Thickness (nm)
	Ar	O_2	Ar/H_2			
A	30	1.5	1.2	2.0	75	205
B	30	1.5	1.2	2.5	54	276
C	30	1.5	1.2	3.0	36	250

The sheet resistance R_{SH} of the as-deposited and annealed films was measured in a 4PP system. **Figure 3.1(a)** and presents R_{SH} values obtained in both sample states (as-deposited and annealed) in function of the power supplied during deposition. The as-deposited films show R_{SH} values below 77 Ω/sq. Upon annealing at 200 ºC, the R_{SH} increases for all samples between 3 and 14-fold. To ensure that the observed variations are not resulting only from the thickness variation, the resistivity was calculated as:

$$\rho = R_{SH} \times t \quad (1)$$

where t is the film thickness. The resulting resistivity **(Figure 3.1(b))** shows a similar behavior as the R_{SH}, indicating that the sputtering power indeed influences the film's electronic properties. From these results, sample B shows the lowest value of R_{SH} for a $P_{density}$=2.5 W/cm^2.

The transmittance of the films was measured in an UV-VIS-MIR spectrometer, and the transmittance spectra of the films are shown in **Figure 3.1(c)**, for the as-deposited (dashed line) and the annealed (solid line) samples. The AVT was obtained from the average of the transmittance data between 380-780 nm, showing transparencies of 86 to 88 %, indicated as labels to the data points in **Figure 3.1a)**. Upon annealing, the AVT increases up to 4 % for the three films. The film with the lowest sheet resistance shows a good AVT of 88% after annealing.

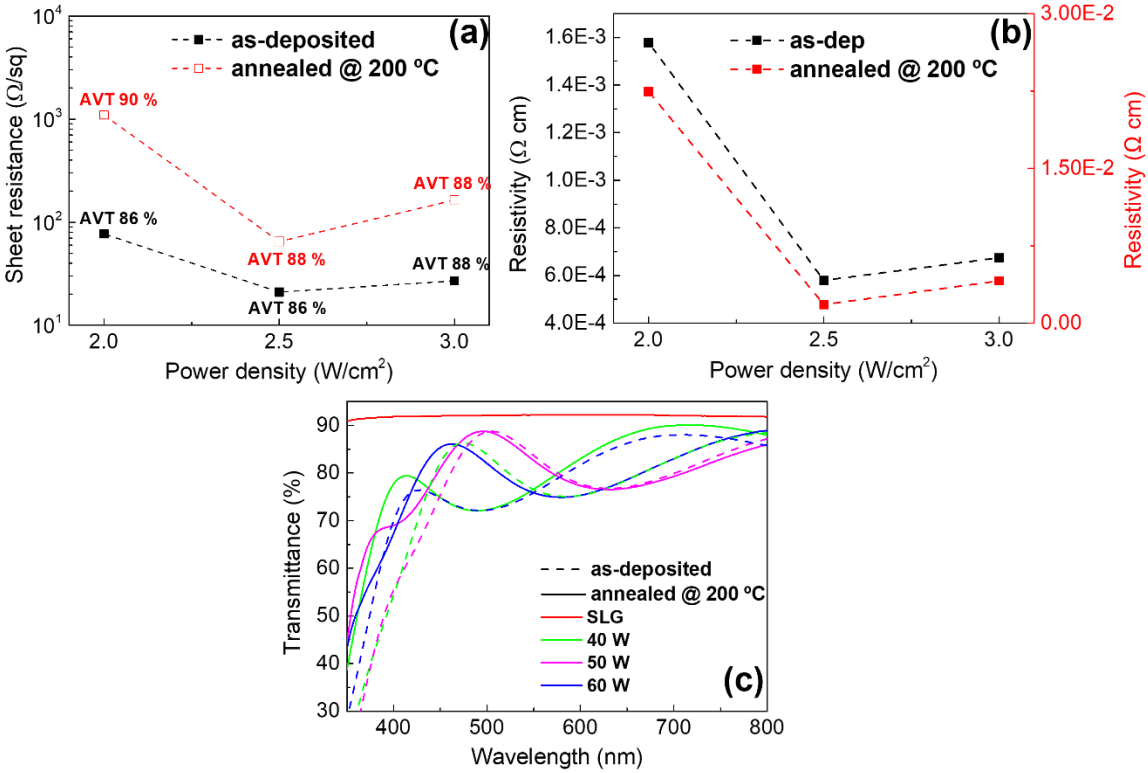

***Figure 3.1**- (a) R_{SH} and (b) resistivity values obtained from 4PP measurements with respective AVT calculated from (c) transmittance spectra for both as-deposited and vacuum annealed samples.*

To investigate any impact of the annealing on the structural properties of the IOH films, XRD characterization before and after annealing was performed. The diffractograms observed **(Figure 3.2)** can be indexed to the cubic structure of In_2O_3 with a lattice parameter of a = 10.13 Å (ICDD card No. 01-080-5364). The structure of the amorphous (as-grown) films, deposited at constant values of H_2 and O_2 content (1.2 and 1.5 sccm, respectively) is presented in **Figure 3.2(a)**. The crystal size for each sample, on the preferred (222) orientation was calculated using the Scherrer's equation, **Eq (2)**:

$$D = \frac{K\lambda}{B\cos(\theta_B)} \quad (2)$$

where D is the average diameter of the crystallites (nm); B is the full width at half maximum (FWHM) and θ_B the peaks' angle (both in radians); K=0.9 as the Scherrer's constant (atoms are considered perfect spheres) and λ=0.154 nm (Cu K_α radiation).

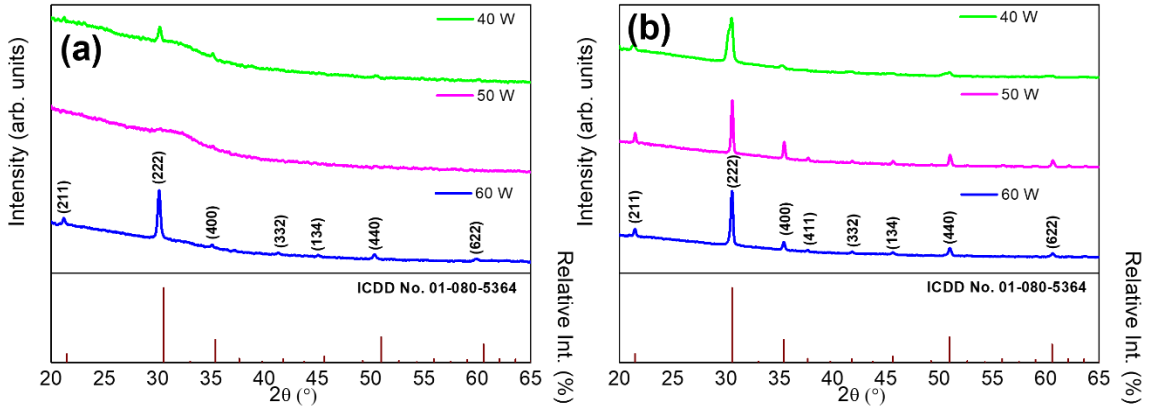

***Figure 3.2**- XRD patterns of (a) as-grown and (b) annealed In_2O_3:H films deposited by reactive RF magnetron sputtering with constant H_2 and O_2 flow and sputter power variation. The In_2O_3 reference pattern was taken from an ICDD database, No. 01-080-5364.*

Samples A and B exhibit a mainly amorphous structure. A few small peaks can be observed for sample A, with the strongest peak at $2\theta \approx 30.2$ º, corresponding to a preferential orientation in the direction (222), indicating the presence of small crystallites inside the amorphous matrix (crystallite size of ~42 nm). The presence of small crystallites indicates an uncontrolled crystallization during deposition which can be attributed to unintentional heating of the substrate by the RF plasma [58]. In contrast, sample B presents a characteristic amorphous structure. On the other hand, sample C shows several diffracted peaks, the strongest one at $2\theta \approx 30.1$ º, indicating again a preferential orientation in the (222) direction. The crystal size can be calculated to 38.0 nm. While fixing the H_2 and O_2 flux, varying the sputtering power can promote the films' crystallinity during deposition [59]. A higher degree of crystallinity was observed for a higher power density of 3.0 W/cm^2. The lattice parameter, a, of the cubic structure of In_2O_3 was calculated using **Eq. (3)**:

$$\frac{1}{d^2} = \frac{h^2 + k^2 + l^2}{a^2} \qquad (3)$$

where h, k and l are the Miller indices of the refracted X-ray and d being the respective interplanar distance. The lattice parameter values, for both as-deposited and annealed samples, are presented as a function of power density in **Figure 3.3**. From the plot data, there is a tendency for as-deposited films to expand the volume of the unit cell with growing power density, thus increasing the lattice constant a. This results in a left-handed shift on the as-deposited XRD diffractograms confirming a lattice relaxation, which can indicate that the H^+ may not be substitutional and instead is staying as an interstitial defect in the crystal network [51], which agrees with Limpijumnong et al. findings, showing that the formation energy (E_f) of interstitial hydrogen (E_f = -2.09 eV) is lower than that of hydrogen on an oxygen site (E_f = -1.40 eV) [60].

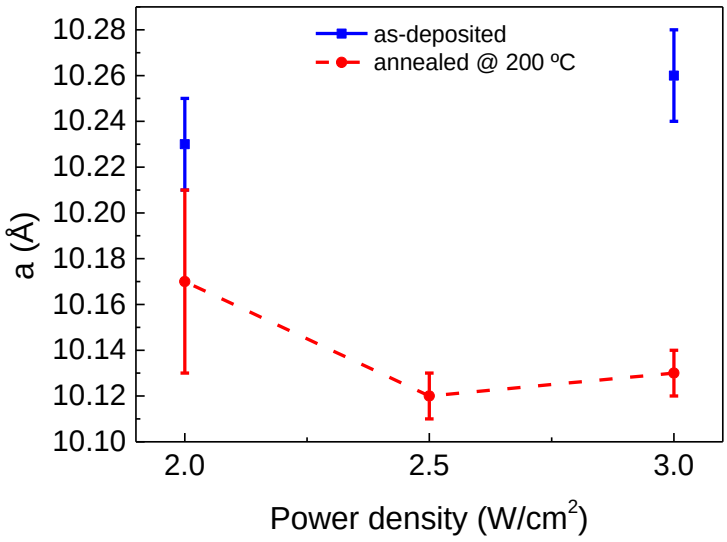

***Figure 3.3**- Lattice parameter, a, as a function of power density, for as-deposited and annealed samples.*

Figure 3.2(b) presents the XRD patterns for the annealed IOH samples in which the solid phase crystallization (SPC) process successfully promoted crystallization of the amorphous phase to a poly-crystalline one with (222) preferred orientation. Sample A shows a double peak in (222) at 2θ≈30.2º and 30.5 º with a slight left shift compared with the reference ICDD card and crystal size of 47.1 nm. Sample B and C show more signs of crystallization with a well-defined (222) peak at 2θ≈30.6 º and 30.5 º and crystal sizes of 59.7 and 52.3 nm, respectively. However, sample B has the narrowest peaks with high intensity showing a good crystalline phase formation, concluding that 50 W can be chosen as a suitable process operating power. Upon annealing, the lattice parameter reduces to values closer to the reference 10.13 Å (**Figure 3.3**), subsequently inducing a right-handed shift on the annealed XRD diffractograms revealing a strained lattice.

3.1.2 Ar/H2 flux variation series

In the second optimization series, the H_2 content was varied fixing the power density value of 2.5 W/cm^2 and using the previous O_2 pulses. Three experimental runs (D, E and F) were performed using different H_2 fluxes: 1.0, 1.2 and 1.4 sccm. After deposition, the films were subjected to a solid-phase crystallization step by heating the substrate to 200 ºC for 1 hour, under high-vacuum conditions (3-4.8×10^{-7} mbar). Sample F was deposited as a reproduction of the optimal parameters studied in the previous section (sample B). The deposition time was adjusted, to maintain the thickness of the samples as constant as possible. **Table 3.2** shows the deposition parameters for these experiments.

Table 3.2 - Deposition parameters for the Ar/H_2 flux variation series.

Sample	Process gases' flux (sccm)			Power Density (W/cm^2)	Time (min)	Thickness (nm)
	Ar	O_2	Ar/H_2			
D	30	1.5	1.0	2.5	54	243
E	30	1.5	1.4	2.5	54	244
F	30	1.5	1.2	2.5	60	278

Figure 3.4 displays the R_{SH} and ρ in function of the H_2 flux, measured in the as-deposited and annealed IOH samples as well as the AVT after SPC.

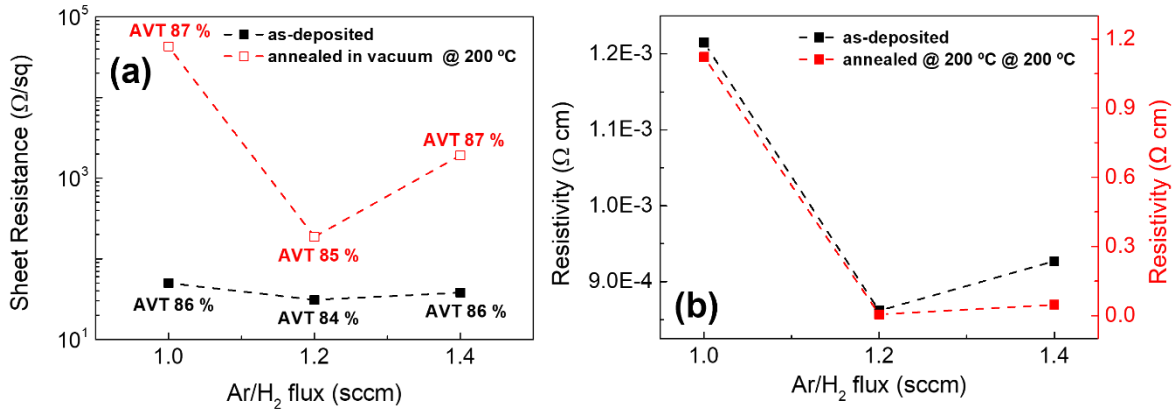

***Figure 3.4**- (a) R_{SH} and (b) resistivity obtained from 4PP measurements with respective AVT for both as-deposited and annealed samples.*

The as-deposited films show R_{SH} values between 31±1.8 and 50±2.5 Ω/sq, with AVT of 84% to 86 %. Upon annealing at 200 ºC, the transmittance values improve by 1 % for all samples. However, the R_{SH} values worsen significantly by up to three orders of magnitude. In terms of optoelectronic properties, the SPC process affects the film's properties, negatively impacting the R_{SH}, as demonstrated by the results obtained before and after annealing, in contrast to literature reports on IOH films [39], [40], [61]. This dramatic change in R_{SH} might be explained by insufficient amounts of H being incorporated into the films which may point that the annealing process or the temperature are not yet optimized, or that the correct process conditions are not yet understood. Specifically, a desorption of gases during annealing could lead to microscopic defects like vacancies, traps or lattice distortions, reducing the H doping and hindering the charge carrier transport [51], [67].

XRD measurements were performed and the respective diffractograms of the annealed samples are presented in **Figure 3.5(a)**. All three samples exhibit a crystalline profile with a preferred (222) orientation like in the previous section, which might be explained by high O_2 partial pressures during

deposition that induce crystalline growth in the (222) orientation [62], thus overpowering the hydrogen introduction as dopant and hindering polycrystalline growth over other preferred orientations like (400). Sample D shows the lowest (222) peak intensity and crystal size of 51±17 nm, with a slight phase segregation and a wide base broadening suggesting that 1.0 sccm of H_2 for the as-deposited process may promote poor crystal quality upon annealing. As the doping level is increased, so does the peak intensity for sample E and sample F as shown in **Figure 3.5(b)**. However, for sample E the peak intensity and crystal size ($D_{E(222)}$ = 52.3 nm) is slightly lower than for sample F ($D_{F(222)}$ = 69.6 nm) indicating that past this threshold, the crystallinity would tend to deteriorate.

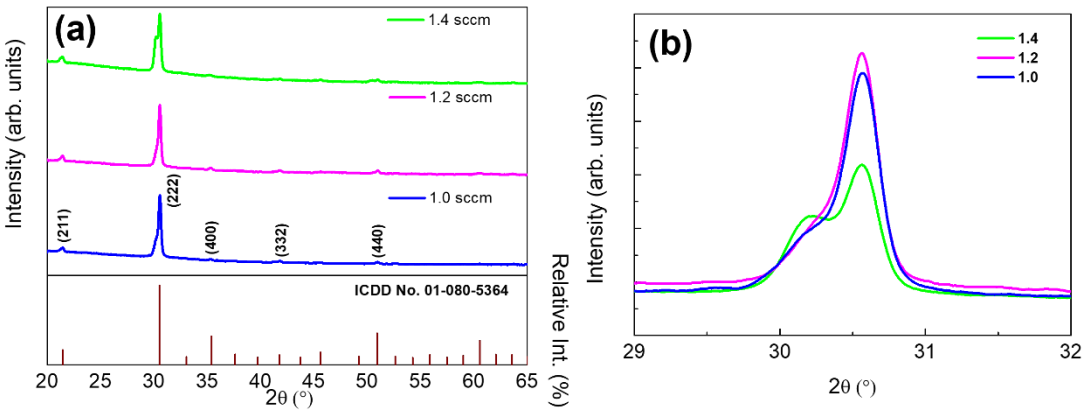

***Figure 3.5**- (a) XRD diffractograms of annealed In_2O_3:H films deposited by reactive RF magnetron sputtering with constant a power density of 2.5 W/cm^2 and H_2 flux variation. (b) High resolution XRD diffractogram for the (222) preferential orientation. The In_2O_3 reference pattern was taken from an ICDD database, No. 01-080-5364.*

The lattice constant was calculated for this optimization series using **Eq. (3)** and plotted as a function of the H_2 flux (**Figure 3.6**).

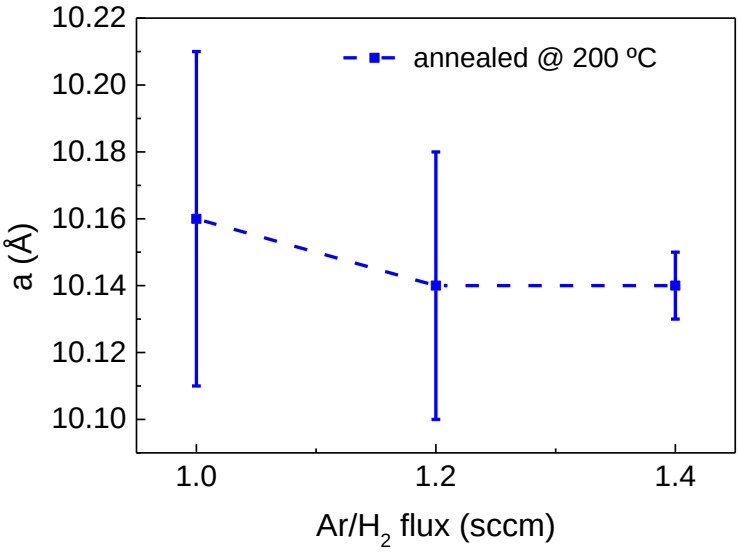

***Figure 3.6**- Crystal lattice parameter, a, as a function of the H_2 flux.*

From the data showed **Figure 3.6**, the lattice parameter, within its experimental variation, tends to decrease with H_2 flux. Some major correlations between the lattice parameters values and their tendency, alongside the H behavior as a dopant in In_2O_3, can be made:

1. Vegard's law dictates a decrease in a as the H_2 content increases. As H^+ has a smaller ionic radius (0.38 Å) [63] than In^{3+} (0.81 Å), the incorporation of H by substitution of In atoms would lead to a very small decrease in the crystal lattice [64]. However, this contradicts the *n*-type conductivity conferred by H^+, as it would work as an acceptor rather than a shallow donor.

2. Within the values spread of a, the tendency to decrease could be explained by a H substitution on the O site [60], thus decreasing the values for a, but the literature still lacks some interpretation of the lattice parameter variation with the hydrogen doping in In_2O_3.

The optical bandgap (E_g) was calculated for all the samples, after the SPC step, using the Tauc plots (**Figure 3.7**) extracted from the absorption coefficient, α (cm^{-1}), in function of the photon energy, hν (eV) . The absorption coefficient and photon energy were determined using the following equations:

$$\alpha = \left(\frac{1}{d}\right) ln\left(\frac{1}{T}\right) \quad (\mathbf{4})$$

where d is the film thickness (cm), and T is the transmittance values obtained from the transmittance spectra.

$$h\nu = \frac{1240\ nm}{\lambda} \quad (\mathbf{5})$$

where h is Planck's constant, ν is the photon frequency and λ is the wavelength of the respective measured transmittance values. Plotting $(\alpha h\nu)^n$ (n=2 for direct interband transitions) in function of hν, E_g is then calculated from the interception of the linear part of the curve with the X axis [65]. **Table 3.3** presents the extracted E_g values.

Table 3.3- Extracted E_g from Tauc plots of **Figure 3.7** with respective film thickness and parameters varied: A, B and C – 40, 50 and 60 W; D, E and F – 1.0, 1.4 and 1.2 sccm.

Sample	Thickness (nm)	E_g (eV)	Parameter variation
Power Series (40, 50 and 60 W)			
A	205	3.33	40
B	276	3.36	50
C	250	3.40	60
H_2 flux series (1.0, 1.2 and 1.4 sccm)			
D	243	3.38	1.0
E	244	3.33	1.4
F	278	3.36	1.2

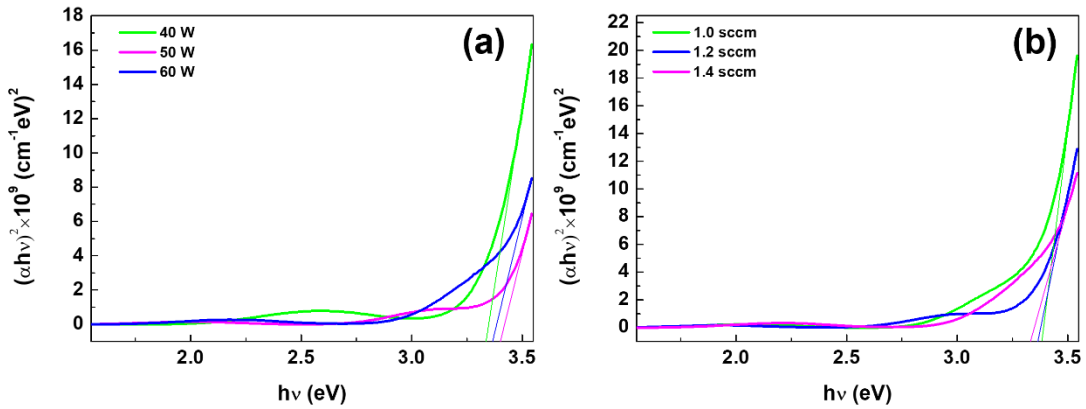

Figure 3.7*- Tauc plots for bandgap estimation from absorption coefficient in function of the photon energy data for annealed (a) power series and (b) H_2 flux series samples.*

3.1.3 CIGSe solar cell back contact deposition and characterization

In this section, an IOH film was sputtered using the deposition conditions identified as optimal in the previous sections, namely 50 W (2.5 W/cm^2) and H_2 and O_2 fluxes of 1.2 and 1.5 sccm, respectively. The R_{SH} value is inversely proportional to the film thickness [66], as shown by **Eq. (1)**, thus the deposition time was increased to 120 min for an expected thickness of ≈ 500 nm, to minimize R_{SH}. During the preparation of the CIGSe layer, temperatures up to 500 ºC are used. Therefore, a preliminary study was performed to understand the impact of such high temperatures on the properties of the IOH film. **Figure 3.8** shows the variation in R_{SH} values with increasing temperature. For the as-deposited state, the film showed a R_{SH} of 9.6±0.6 Ω/sq and an AVT of 78 %. Upon vacuum annealing at 200 ºC, both the R_{SH} and AVT improve to 7.26±0.1 Ω/sq and 81 %, respectively. This R_{SH} behavior is not concordant with the values obtained in the previous sections but is in agreement with literature reports [20]. To test how the selenization temperature would influence the film's properties, an inch-by-inch piece of the IOH sample was cut and selenized at 500 ºC (conditions described in section 2.3). The R_{SH} suffers from a major increase in value of about 4 orders of magnitude when compared to the annealed state, in agreement with a report by Koida et al., where the electrical properties were observed to deteriorate for T ≥ 400 ºC [50]. Wardenga et al., stated a loss in carrier mobility associated with H removal during the annealing due to higher transport barriers for electrons at the grain boundaries hindering the passivation effect of H at these sites [67]. It is also proposed that Se incorporated during selenization is found inside the grain boundaries after absorber deposition, significantly increasing the sheet resistance by a factor of 3.

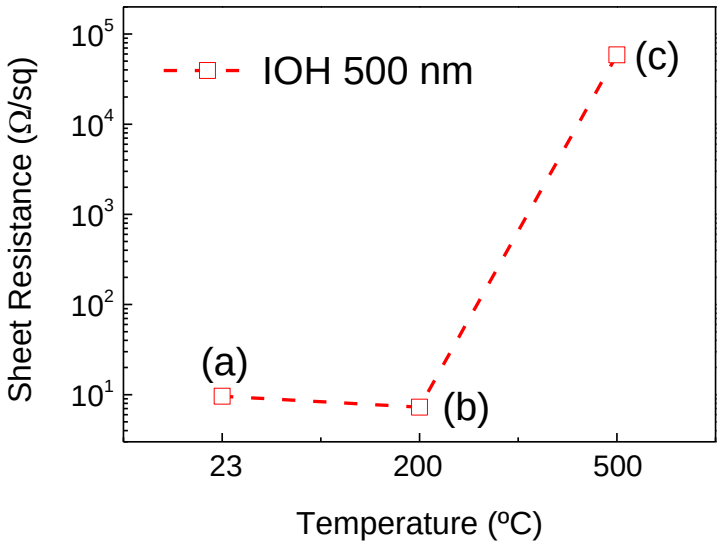

Figure 3.8- *R_{SH} values in function of the temperature conditions of each process: (a) deposition of the as-deposited (~23 ºC) state with no intentional heating; (b) after annealing at 200 ºC and (c) post-selenization at 500 ºC.*

XRD measurements were performed for post-deposition, annealing and selenization to study the temperature influence in the structural properties of the sputtered IOH film. **Figure 3.9** presents the obtained diffractograms.

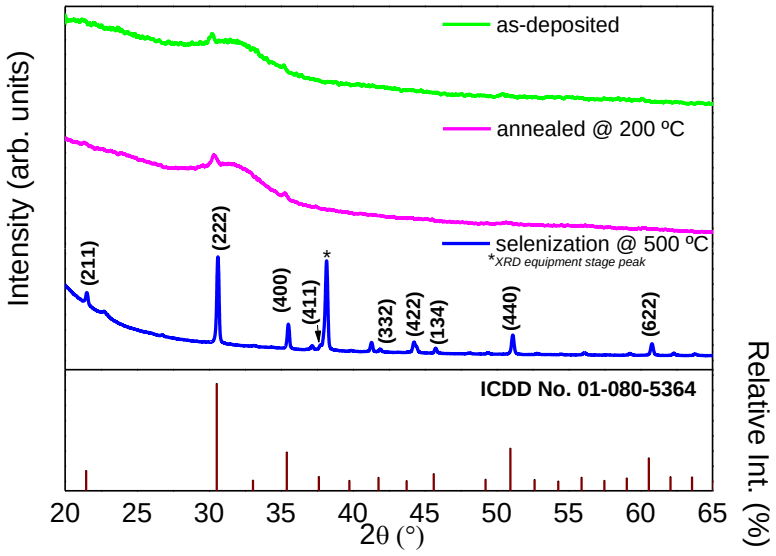

Figure 3.9- *XRD diffarctograms of an IOH sample for the as-deposited state, annealing at 200 ºC and selenization at 500 ºC. The In_2O_3 reference pattern was taken from an ICDD database, No. 01-080-5364*

The XRD patterns of the as-deposited IOH film presented low diffraction intensity at (222) and (400) orientations and a rather broad background, without any intentional compositional variation, suggesting that the film is composed by both crystalline and amorphous materials, when deposited. Upon vacuum annealing, the film still shows a broad background characteristic of the amorphous state but with hardly noticeable improvement on the peak formation for (222) and (400) orientations. The crystal size also slightly increased from 14.3 (as-deposited) to 17.1 nm (vacuum annealing at 200 ºC). This type

of structural change reinforces the need to better understand the annealing step and the practical conditions applied during the process as a crystalline development was to be expected represented by a peak intensity enhancement throughout the diffractogram. As identified in **Figure 3.9**, the presence of a diffraction peak for $2\theta \approx 38.2$ º corresponds to the stage from the XRD equipment due to the sample's reduced area. For the post-selenization state, the XRD patterns reveals well defined diffraction peaks along the major In_2O_3 orientations [(222), (400), (440) and (622)] with corresponding peaks at $2\theta \approx$ 30.6, 35.5, 51.1 and 60.8 º, respectively, and a large increase in crystal size from 17.1 to 57.2 nm in the (222) preferential orientation.

3.2 IOH and Mo based CIGSe solar cells

This section describes the results on two CIGSe solar cells with different back contacts. Both solar cells were fabricated using a substrate configuration with an IOH based TBC and a reference cell using a conventional Mo back contact. Both back contacts were deposited with a targeted thickness of 500 nm. The IOH film used was previously described in section 3.1.3 and a conventional Mo bi-layer was deposited by direct-current magnetron sputtering as the reference cell back contact. The absorber layer was deposited with a thickness of ~2 μm. The post-selenization, KCN etching treatment, CBD of the buffer layer and window layer deposition were previously described in section 2.3.

Figure 3.10(a) depicts the XRD patterns of the CIGSe absorber layer on the two different back contacts (IOH and Mo). As observed before, the diffraction peak at $2\theta \approx 38.2$ º corresponds to the stage of the XRD equipment due to the sample's reduced area. For the IOH based solar cell, the XRD pattern shows the major diffraction peaks related to the In_2O_3 with preferential (222) orientation, whereas for the reference cell, a characteristic sharp peak in the (110) orientation at $2\theta \approx 40.5$ º, confirms the presence of Mo in the cell structure. A peak at $2\theta \approx 34.3$ º, also identified in the Mo based solar cell spectra, infers about the presence of Se into the crystal structure of the selenized cell stacks. Keller et al., stated that the presence of Se at the grain boundaries was attributed as a major cause for the detrimental electrical performance of IOH films [20]. In **Figure 3.10(b)** a comparison between both solar cells diffraction peaks at the preferential orientation (112) is presented. The most intense peak corresponds to the Mo reference cell. The (112) orientation peak intensity and crystal growth tends to be influenced by the presence of sodium, which indicates that the Na diffusion from the SLG to the absorber layer is more pronounced when Mo is used than IOH [20], [68].

The presence of a ternary $CuInSe_2$ (CIS) phase and quaternary (CIGSe) phase is visible as the major intensities identified from the chalcopyrite material present double peaks. This type of phase segregation often occurs for both ternary phases like CIS and $CuGaSe_2$ (CGS) which depends on process time and whether selenization temperatures are low (for CIS) or high (for CGS) [69]. Dittrich et al., stated that for a process time of 90 min and a temperature of 450 ºC a CGS phase was achieved, whereas for the same process duration at 400 ºC a CIS phase was formed. Moreover, this CIS phase could have been accomplished with only 30 min of reaction time at the same temperature value, concluding that the CIS ternary phase forms much faster than the CIGSe quaternary phase and consequently the CGS [70].

XRD data from **Figure 3.10(a)** shows that the selenization process used in this study did not promote CGS formation. Nevertheless, CIGSe diffraction peaks, though in lesser intensity, are present in our absorber material for both solar cells. This evidence states that a better adaptation of the selenization temperature and a possible process optimization for these specific absorber deposition conditions may be needed to better patronize the quaternary phase of CIGSe.

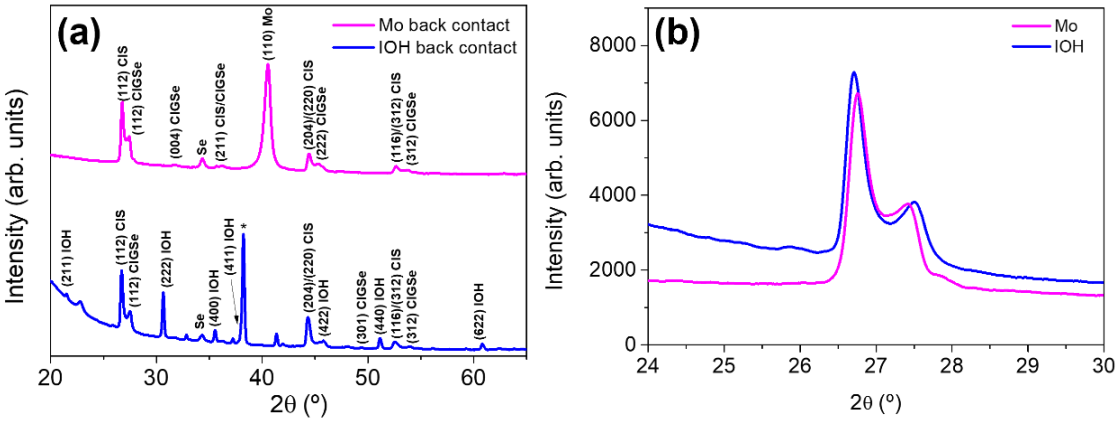

Figure 3.10- *(a) XRD diffractograms of two fabricated solar cells containing two different back contacts: an IOH based solar cell and a reference solar cell containing a conventional Mo bi-layer (* represents a stage peak due to the sample's small area). (b) High resolution XRD diffractogram for the (112) preferential orientation of CIS and CIGSe.*

Quantification of the bulk elemental concentrations of Cu, In, Ga and Se for each solar cell absorber was obtained by EDX (at 20 keV) analysis through top surface SEM imaging using the mean values of several point measurements. The CGI and GGI ratios were also calculated through the expressions referred in section 1.2. These experimental values are listed in **Table 3.4.**

Table 3.4- Chemical composition of the CIGSe absorber (Cu, In, Ga and Se, at %) and respective CGI and GGI ratios, for both IOH and Mo back contact based solar cells, after KCN etching.

Cell back contact	Cu (at %)	In (at %)	Ga (at %)	Se (at %)	CGI ratio	GGI ratio
IOH	20.3±3.3	15.0±1.5	16.5±6.9	48.2±4.0	0.6	0.5
Mo	21.5±1.5	23.6±3.8	10.5±1.8	44.8±0.2	0.6	0.3

The absorber layer presents a Cu-poor composition for both solar cells, ranging from 20.3% for the IOH based solar cell and 21.5 % for the Mo reference cell. The KCN etching treatment removes $Cu_{2-x}Se$ formed at the surface of the film, which also affects the chemical composition of Cu and Se. The CGI and GGI ratios come into play since both tune important prospects such as crystal growth (CGI) and the absorber bandgap (GGI). The bandgap dependence on the GGI ratio is given by the following equation [75]:

$$E_g(x) = (E_g^{CGS}x) + \left[E_g^{CIS}(1-x)\right] - [bx(1-x)] \quad (6)$$

where x is the GGI ratio, E_g^{CGS}-1.68 eV, E_g^{CIS}-1.04 eV, and b is the deflection coefficient (at room temperature, b=0.12). The bandgap values for the IOH and Mo based solar cells were calculated to be 1.33 and 1.21 eV, respectively. As the IOH based cell presents a higher atomic concentration of Ga it is expected to have a higher bandgap than the cell with Mo. The Mo cell presents a mean GGI ratio of 0.3 which is the ideal composition to achieve high efficiency solar cells. Both cells present a mean value of CGI ratio of 0.6 which is below the value suggested as optimal in the literature, which would be between 0.75-0.95 [71]. Despite the good GGI composition of the Mo reference cell, to use CIGSe as a top cell for tandem or bifacial applications, wider bandgap absorbers are required (~1.7 eV), thus increasing the GGI ratio and tuning of the deposition process is necessary.

SEM cross section images were taken to infer about the structure of the fabricated devices. **Figure 3.11** depicts the cross-sectional views of the IOH based device and the Mo reference cell. Closely inspecting the SEM cross sectional images, there is an evident crystalline growth of the absorber layer with the selenization for both cells. The IOH and Mo back contacts are present in the device stack and showing good adhesion with the CIGSe absorber. However, on the top images of **Figure 3.11**, some crystallites close to the IOH back contact show a different morphology (indicated by the red circles). Keller et al., stated that a highly resistive and typically amorphous Ga_2O_3 layer may form upon CIGSe high temperature deposition, at the TBC/absorber interface, creating additional barriers for hole extraction. Ga_2O_3 also shows n-type conductivity and can form, along with p-type CIGSe, a reverse p-n junction at the back contact interface which opposes the main current coming from the p-n junction at the absorber/buffer site, thus hindering the solar cell performance [19]. Moreover, it has been stated that Ga_2O_3 is thermodynamically favorable when growing CIGSe on top of IOH due to high temperature deposition [20]. A thorough investigation via EDX and characterization by higher resolution techniques such as transmission electron microscopy (TEM) is needed to better analyze the TBC/CIGSe interface. X-ray photoelectron spectroscopy (XPS) would also provide a sensitive method to distinguish Ga from the absorber from Ga_2O_3 since the binding energy of Ga decreases when changing from an oxidized state to the Ga present in the absorber bulk [73].

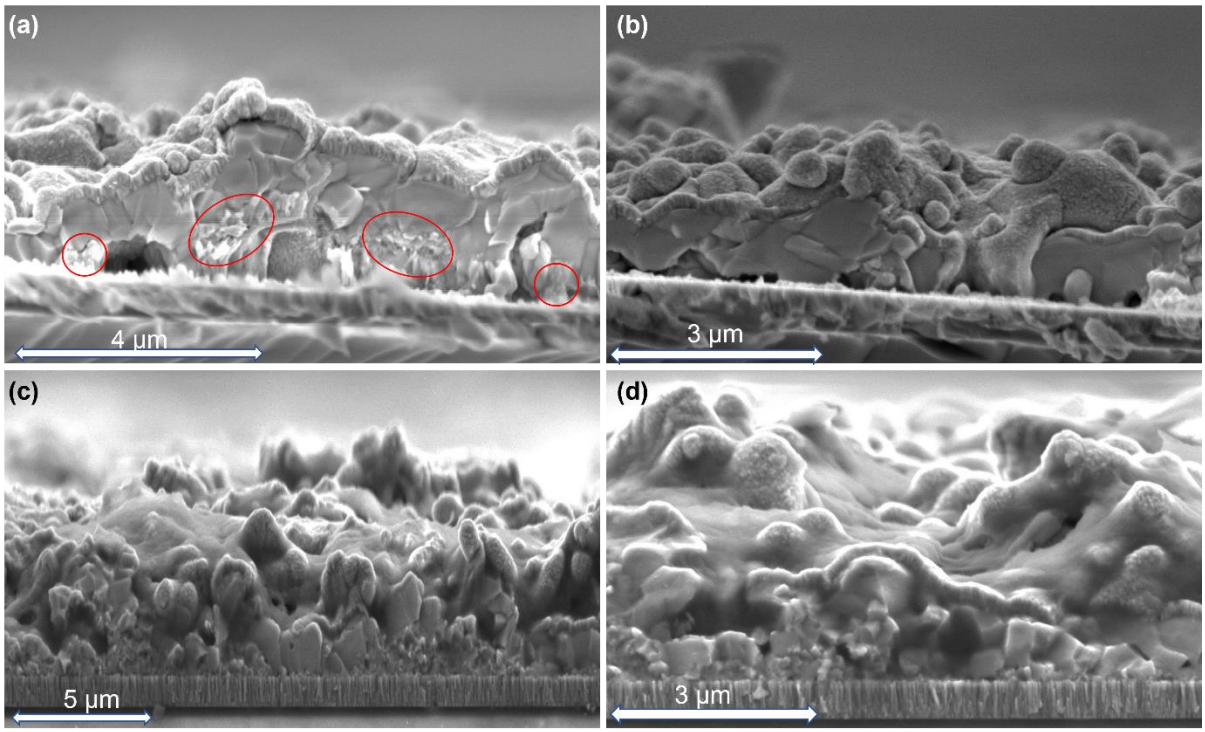

Figure 3.11- *SEM cross section views of the back contact interface with CIGSe for (a,b) IOH TBC/CIGSe and (c,d) for Mo/CIGSe. Red circles represent a different morphology present at the IOH interface with the absorber layer, suspected to be* Ga_2O_3.

3.2.1 *JV measurements and solar cell performance characterization*

As described in section (1.1), a solar cell can generate a current and a voltage through the photovoltaic effect and the use of a semiconductor material to efficiently collect charge carriers. By plotting the current in function of the voltage, an *I-V* curve is obtained containing valuable information about the device performance i.e., open-circuit voltage (V_{OC}) and short-circuit current (I_{SC}), short-circuit current density (J_{SC}), fill factor (FF) and power conversion efficiency (PCE). Solar cells also exhibit two

types of ohmic resistances: series (R_S) and shunt (R_{SHUNT}) resistances. Minimizing R_S is essential since high R_S values can affect the fill factor and short-circuit current. Point defects in the p-n junction, pin-holes, impurities from the material lattice and leaking currents influence the shunt resistance values. Thus, maximizing R_{SHUNT} is essential since low R_{SHUNT} can provide alternative current paths, reducing the output power [72].

The fabricated solar cells were divided into sub cells with areas between 0.016 – 0.021 cm^2, using mechanical scribing with a needle. The *I-V* characteristics for each sub cell were obtained in a solar simulator under a total irradiance of 0.097 W/cm^2. **Figure 3.12** presents the respective measured *I-V* curves for each device.

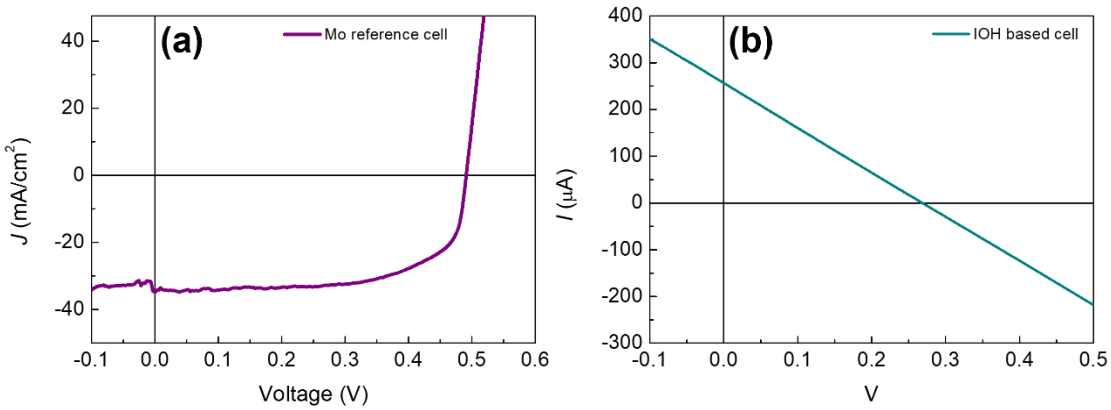

Figure 3.12- *(a) J-V characteristic curve for the Mo reference solar cell. (b) I-V curve with a resistive behavior for the IOH based solar cell.*

Having measured the *I-V* parameters of the Mo reference cell, the obtained curves for each sub cell presented some background noise due to poor contact with the probe tips. To ensure a correct analysis of the curves, a smoothing of the noisy profile was performed, alongside a recalculation of the ohmic resistances to assure more accurate data. Using a linear fit when at V_{OC} = 0 and I_{SC} = 0 allows to obtain the values for R_S and R_{SHUNT}. Other important parameters such as J_{SC}, FF and the PCE were corrected in function of the new fitted values, using the following equations:

$$J_{SC} = \frac{I_{SC}}{A} \tag{7}$$

$$P_{max} = I_{max} V_{max} \tag{8}$$

$$FF = \frac{P_{max}}{V_{OC}\, I_{SC}} \times 100 \tag{9}$$

$$PCE = \frac{FF\, I_{SC} V_{OC}}{A I_{AM1.5}} \times 100 \tag{10}$$

where, A is the cell area (cm^2); P_{max} is the maximum generated power (W) and $I_{AM1.5}$ is the integrated power of the AM1.5 global spectrum (considered as 0.1 W/cm^2 but in this case as 0.097 W/cm^2).

The best Mo based solar cell presented a V_{OC}=0.49 V; J_{SC}=33.4 mA/cm^2; FF=68 % and PCE=11.5 %. A characteristic *I-V* curve was measured for the reference cell whereas the IOH back contact did not lead to a working device, which contradicts what is reported in the literature [12], [20], [21]. SEM cross section (see section 3.1.3) showed a similar CIGSe growth for both cells with well-

defined crystals inside the cell structure, thus the CIGSe deposition is not the major factor to consider, as the Mo reference cell shows good *I-V* parameters (**Table 3.5** and **Figure 3.13**). **Figure 3.12(b)** shows a typical resistive curve with a fast current decline with the voltage. From the analysis in the previous section, we could identify high temperature selenization as detrimental to the film's electrical properties. Moreover, this device presents a mean value of series resistance of 5498 Ω. As stated before, the series resistance influences the output current values as well as the FF of the device and should be minimized. Coupled with a pronounced increase of the R_{SH} of IOH, upon selenization, the FF of the IOH based cell was affected thus presenting a resistive behavior.

Table 3.5- Average and best solar cell *I-V* parameters (open-circuit voltage, V_{OC}; short-current density, J_{SC}; fill factor, *FF*; power conversion efficiency, PCE; series resistance, R_S and shunt resistance, R_{SHUNT}) obtained for a Mo back contact reference solar cell.

Back contact		**V_{OC} (V)**	**J_{SC} (mA/cm^2)**	**FF (%)**	**PCE (%)**	**R_S (Ω)**	**R_{SHUNT} (Ω)**
Mo	Average	0.51±0.01	23.6±5.8	77.4±4.5	9.7±1.9	2.8±0.8	4527±4274
	Best cell	0.49	33.4	68	11.5	3.41	1755

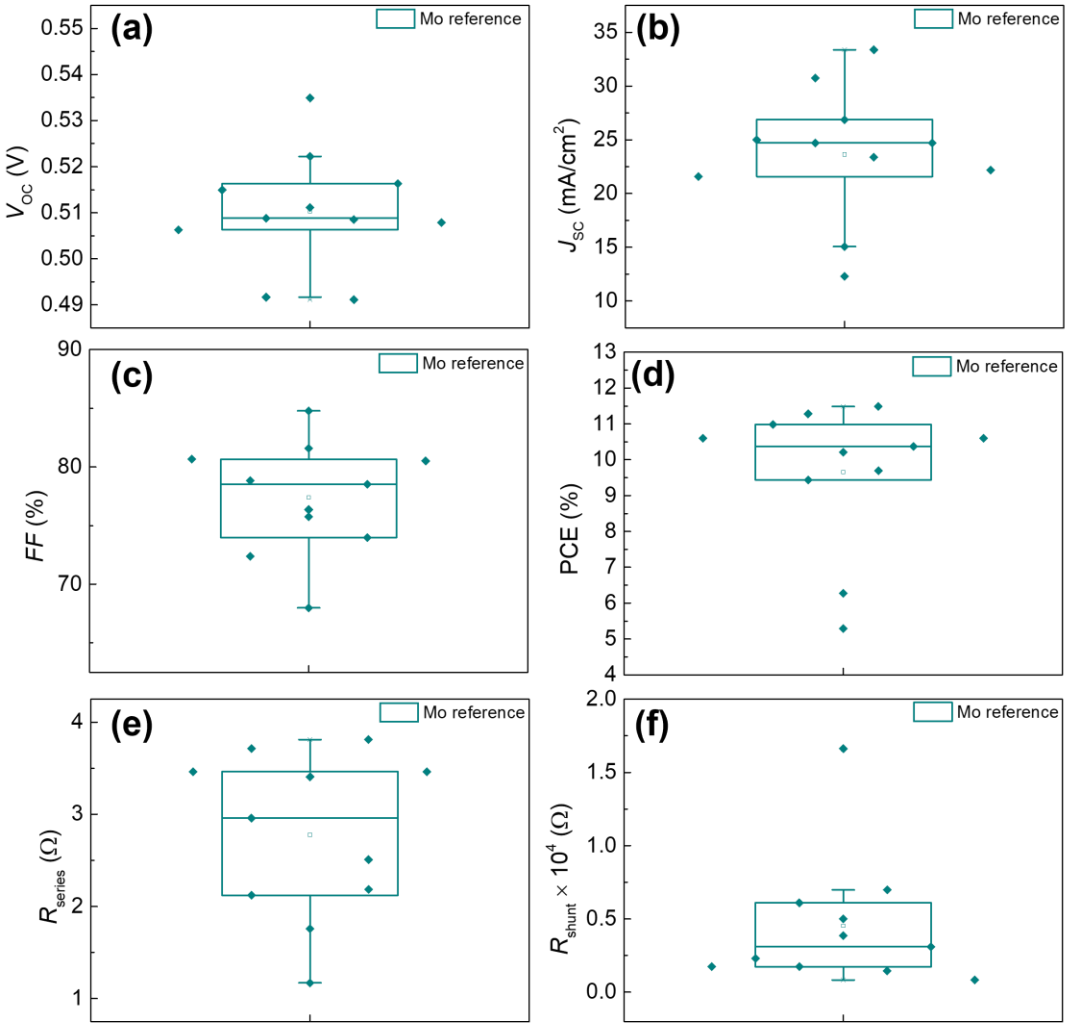

Figure 3.13- *Box plot of (a) open-circuit voltage, (b) short-current density, (c) fill factor, (d) power conversion efficiency, (e) series and (f) shunt resistances for the reference CIGSe solar cell using a Mo back contact.*

IOH does not permit the same amount of Na diffusion as Mo [20]. Na is a key component of high performance CIGSe solar cells and is required for Cu-poor films to improve V_{OC} and FF. Solar cells using TBC instead of Mo often show a pronounced reduction in fill factor, potentially catalyzed by an increase in sheet resistance values upon selenization, which results in an increased series resistance. Keller et al., showed that the deposition of a very thin resistive layer (~5 nm) of aluminum oxide (Al_2O_3) can improve the back contact interface with CIGSe when in the presence of Ga_2O_3. The Al_2O_3 layer reduced the probability of recombination at the back contact by either passivating the junction or preventing a Ga depletion in that region, leading to an increased collection efficiency for electrons generated close to the IOH. This layer also reduces excessive Na diffusion, when sodium fluoride (NaF) post deposition treatment (PDT) is performed, which promotes Ga_2O_3 formation.

4

CONCLUSION AND FUTURE PERSPECTIVES

This work focused on the optimization of a sputtering deposition process for hydrogen-doped indium oxide to serve as a back contact for bifacial and tandem solar cells applications. Molybdenum is the standard solar cell back contact for CIGSe based devices, however, its opaque nature prevents the semi-transparency required for these applications. It is proposed that TCOs have the right optoelectronic properties to overcome this adversity. A two-step process introduced by Koida, consists in growing amorphous films without any intentional heating. Then, a solid-phase crystallization step with annealing of the IOH in vacuum at 200 ºC is utilized to confer polycrystallinity to the as-grown films. Process parameters like oxygen and hydrogen flux are key to obtain high quality films and to control undesired crystallinity during the as-deposited state. Oxygen and hydrogen are also responsible for tuning the optoelectronic properties of the films, so it is of high importance to learn how to balance their stoichiometry during films deposition, which proved to be quite a challenge since very low fluxes were required. Firstly, the sputtering power variation was studied. As-deposited films were obtained with some of them showing crystallinity in some preferred orientations. While fixing the H_2 and O_2 content, increasing the sputtering power can promote the films' crystallinity during deposition, due to higher kinetic energy sputtering atoms that will favor the rearrangement of atoms into more stable structures. A sputtering power density of 2.5 W/cm^2 was chosen as the optimal value for the subsequent depositions. Hydrogen plays an important role in these depositions since H^+ is the source of *n* conductivity in the IOH films and can act as either an interstitial or substitutional impurity, reducing the free carrier density and improving film's electrical properties.

Although the crystallinity is improved, the R_{SH} is affected by the SPC process, stressing that the annealing step or the process conditions are not fully understood yet. A loss of hydrogen during annealing or very low flux could also be considered as major limitations for the electrical properties. Thus, an optimization of the annealing parameters like temperature and pressure and a better control of the dopant insertion is recommended for future work in this topic. Further optimization showed that the increase in the IOH film thickness can directly reduce the R_{SH} values. However, this comes with a tradeoff in the AVT values reducing its overall transparency.

Upon absorber deposition, the IOH film was subjected to a selenization process at 500 ºC to achieve a highly efficient CIGSe layer. This process proved to worsen further the R_{SH} value by up to 4 orders of magnitude. Such behavior was evidenced by Koida, who stated that IOH electrical properties tend to deteriorate when exposed to temperatures above 400 ºC. Moreover, a pure Se peak in the XRD pattern might infer about incorporation of this element at the grain boundaries, thus worsening the film's performance. A phase segregation of CIS and CIGSe is evidenced by the XRD analysis due to an insufficient temperature regulation during the selenization process which promoted a more In rich phase of the chalcopyrite material. Elemental composition from EDX revealed a good value of the GGI ratio of 0.3 (within high efficiency range) for the Mo reference cell. Although the CGI ratios for both cells (0.6) are below the ideal range stated in the literature, a Cu-poor profile (requisite for high efficiency CIGSe solar cells) was achieved.

The solar cells characteristic parameters were extracted as their respective *I-V* curves. A Mo reference cell with V_{OC}=0.49 V; J_{SC}=33.4 mA/cm^2; FF=68 % and PCE=11.5 % was achieved. However, the IOH based device failed to provide working solar cells, which exhibited *I-V* curves with resistive behavior. Cross sectional SEM images for both devices showed a good development of the absorber layer upon selenization, with a good layer consistency and the formation of large crystals. However, from the results of **Figure 3.8,** a high temperature selenization and a possible loss of hydrogen doping resulted in a very resistive IOH film. Moreover, it is hypothesized that formation of a Ga_2O_3 layer around the grains near the back contact/absorber interface might be responsible for the poor performance of the IOH based device. Keller et al., proposed the deposition of a very thin layer of Al_2O_3 in conjunction with an optimized NaF PDT, which showed overall improvement on the back contact/absorber interface in the presence of Ga_2O_3 as well as in the *I-V* parameters of the solar cell.

Further improvement of these CIGSe devices can be made by a 3-stage co-evaporation process deposition of individual elements at temperatures above 550 ºC. Deposition of wider bandgap CIGSe rather than decreasing its thickness will enhance device transparency, while maintaining good efficicencies. To better comprehend the TBC/CIGSe interface and the IOH films composition and optoelectronic properties, powerful characterization techniques like TEM, XPS and Kelvin probe force microscopy (KPFM) must be considered.

5

REFERENCES

[1] S. Eslami, A. Gholami, A. Bakhtiari, M. Zandi, and Y. Noorollahi, “Experimental investigation of a multi-generation energy system for a nearly zero-energy park: A solution toward sustainable future,” *Energy Convers. Manag.*, vol. 200, pp. 107–112, 2019.

[2] J. J. M. Halls *et al.*, “Efficient photodiodes from interpenetrating polymer networks,” *Letters to nature*, vol. 50. pp. 1–3, 1995.

[3] ISE 2021 Photovoltaics Report - Prepared by Fraunhofer Institute for Solar Energy System, 2022.

[4] K. L. Chopra, P. D. Paulson, and V. Dutta, “Thin-film solar cells: An overview,” *Prog. Photovoltaics Res. Appl.*, vol. 12, pp. 69–92, 2004.

[5] J. Sun and J. J. Jasieniak, “Semi-transparent solar cells,” *J. Phys. D. Appl. Phys.*, vol. 50, pp. 28, 2017.

[6] S. Zhang and N. Ali, "Nanocomposite thin films and coatings: Processing, properties and petformance," *Imperial College Press*, 978-1-86094-784-1, pp. 381-410, 2007.

[7] G. Conibeer, “Third-generation photovoltaics,” *Mater. Today*, vol. 10, pp. 42–50, 2007.

[8] M. Hossain, U. W. Paetzold, B. S. Richards, and H. Kalt, “Semitransparent perovskite solar cells for perovskite-based tandem photovoltaics,” KIT, 2020, Master Thesis Dissertation.

[9] G. E. Eperon and H. J. Snaith, “Metal halide perovskite tandem and multiple-junction photovoltaics,” *Nat. Rev.*, vol. 1, pp. 1–18, 2017.

[10] M. H. Futscher and B. Ehrler, “Efficiency Limit of Perovskite/Si Tandem Solar Cells,” *ACS Energy Lett.*, vol. 1, pp. 863–868, 2016.

[11] M. J. Shin *et al.*, “Semi-transparent photovoltaics using ultra-thin Cu(In,Ga)Se2 absorber layers prepared by single-stage co-evaporation,” *Sol. Energy*, vol. 181, pp. 276–284, 2019.

[12] J. Keller, W. C. Chen, L. Riekehr, T. Kubart, T. Törndahl, and M. Edoff, “Bifacial Cu(In,Ga)Se2 solar cells using hydrogen-doped In2O3 films as a transparent back contact,” *Prog. Photovoltaics Res. Appl.*, vol. 26, pp. 846–858, 2018.

[13] M. Nakamura, K. Yamaguchi, Y. Kimoto, Y. Yasaki, T. Kato, and H. Sugimoto, “Cd-Free Cu (In , Ga)(Se , S) 2 Thin-Film Solar Cell With Record Efficiency of 23 . 35 %,” *IEEE*, vol. 9, pp. 1863–1867, 2019.

[14] K. H. Ong *et al.*, “Review Article Review on Substrate and Molybdenum Back Contact in CIGS Thin Film Solar Cell,” *Int. J. Photoenergy*, vol. 9106269, pp. 1–14, 2018.

[15] P. T. Erslev, A. Halverson, W. Shafarman, and J. D. Cohen, “Study of the Electronic Properties of Matched Na-Containing and Reduced-Na CuInGaSe 2 Samples Using Junction Capacitance Methods,” *Mater. Res. Soc. Symp. Proc.*, vol. 1012, pp. Y12–Y30, 2007.

[16] F. Liu *et al.*, “Emerging inorganic compound thin fi lm photovoltaic materials : Progress , challenges and strategies,” *Mater. Today*, vol. 41, pp. 120–142, 2020.

[17] R. J. Matson *et al.*, “Metal contacts to CuInSe2,” *Sol. Cells*, vol. 11, pp. 301–305, 1984.

[18] K. Orgassa, H. W. Schock, and J. H. Werner, “Alternative back contact materials for thin film Cu(In,Ga)Se2 solar cells,” *Thin Solid Films*, vol. 431–432, pp. 387–391, 2003.

[19] T. Nakada, Y. Hirabayashi, T. Tokado, D. Ohmori, and T. Mise, “Novel device structure for Cu(In,Ga)Se2 thin film solar cells using transparent conducting oxide back and front contacts,” *Sol. Energy*, vol. 77, pp. 739–747, 2004.

[20] J. Keller, L. Stolt, O. Donzel-Gargand, T. Kubart, and M. Edoff, “Wide-Gap Chalcopyrite Solar Cells with Indium Oxide–Based Transparent Back Contacts,” *Sol. RRL*, vol. 2200401, pp. 1–13, 2022.

[21] J. Keller *et al.*, “Using hydrogen-doped In2O3 films as a transparent back contact in (Ag,Cu)(In,Ga)Se2 solar cells,” *Prog. Photovoltaics Res. Appl.*, vol. 26, pp. 159–170, 2018.

[22] C. Su, W. Ho, H. Lin, C. Nieh, and S. Liang, “Solar Energy Materials & Solar Cells The effects of the morphology on the CIGS thin films prepared by CuInGa single precursor,” *Sol. Energy Mater. Sol. Cells*, vol. 95, pp. 261–263, 2011.

[23] J. F. Guillemoles, “The puzzle of Cu (In , Ga) Se 2 (CIGS) solar cells stability,” *Thin Solid Films*, vol. 404, pp. 405–409, 2002.

[24] S. B. Zhang, S. Wei, and A. Zunger, “Defect physics of the CuInSe 2 chalcopyrite semiconductor,” *Phys. Rev. B - Condens. Matter Mater. Phys.*, vol. 57, pp. 9642–9656, 1998.

[25] Y.-C. Wang and H.-P. D. Shieh, “Double-graded bandgap in Cu (In , Ga) Se 2 thin film solar cells by low toxicity selenization process,” *Appl. Phys. Lett.*, vol. 073901, pp. 1–4, 2014.

[26] U. Rau *et al.*, “High Quality Baseline for High Efficiency, Cu(In 1,” *Prog. Photovoltaics Res. Appl.*, vol. 15, pp. 507–519, 2007.

[27] P. Jackson, R. Wuerz, D. Hariskos, E. Lotter, W. Witte, and M. Powalla, “Effects of heavy alkali elements in Cu (In , Ga) Se 2 solar cells with efficiencies up to 22 . 6 %,” *Phys. Status Solidi RRL*, vol. 586, pp. 583–586, 2016.

[28] M. Kemell, M. Ritala, and M. Leskelä, “Thin film deposition methods for CuInSe2 solar cells,” *Crit. Rev. Solid State Mater. Sci.*, vol. 30, pp. 1–31, 2005.

[29] J. Qu, L. Zhang, H. Wang, X. Song, Y. Zhang, and H. Yan, “Simulation of double buffer layer on CIGS solar cell with SCAPS software,” *Opt. Quantum Electron.*, vol. 51, pp. 1–14, 2019.

[30] L. L. Kazmerski, F. R. White, and G. K. Morgan, “Thin-film CuInSe 2 / CdS heterojunction solar cells,” *Appl. Phys. Lett.*, vol. 268, pp. 27–30, 1976.

[31] K. Mitchell, R. Potter, J. Ermer, R. Wieting, and C. Eberspacher, “High efficiency thin film tandem PV modules,” *Photovolt. Spec. Conf.*, vol. A88-34226, pp. 13–18, 1987.

[32] H. I. Abdalmageed, M. Fedawy, and M. H. Aly, “Effect of absorber layer bandgap of CIGS-based solar cell with (CdS / ZnS) buffer layer Effect of absorber layer bandgap of CIGS-based solar cell with (CdS / ZnS) buffer layer,” *J. Phys. Conf. Ser.*, vol. 2128, pp. 1–9, 2021.

[33] T. Minemoto *et al.*, “Theoretical analysis of the effect of conduction band offset of window / CIS layers on performance of CIS solar cells using device simulation,” *Sol. Energy Mater. Sol. Cells*, vol. 67, pp. 83–88, 2001.

[34] M. L. Cohen and J. R. Chelikowsky, *Electronic Structure and Optical Properties of Semiconductors*, 978-3-642-97082-5, pp. 161-171, 1988.

[35] K. L. Chopra, S. Major, and D. K. Pandya, “Transparent conductors-A status review,” *Thin Solid Films*, vol. 102, pp. 1–46, 1983.

[36] T. Minami, K. Oohashi, and S. Takata, “Preparations of ZnO:Al transparent conducting films by d.c. magnetron sputtering,” *Thin Solid Films*, vol. 194, pp. 721–729, 1990.

[37] R. Das and S. Ray, “Zinc oxide - A transparent, conducting IR-reflector prepared by rf-magnetron sputtering,” *J. Phys. D. Appl. Phys.*, vol. 36, pp. 152–155, 2003.

[38] Y. Igasaki and H. Kanma, “Argon gas pressure dependence of the properties of transparent conducting ZnO : Al ® lms deposited on glass substrates,” *Appl. Surf. Sci.*, vol. 169–170, pp. 508–511, 2001.

[39] T. Koida, H. Fujiwara, and M. Kondo, “Hydrogen-doped in2O3 as high-mobility transparent conductive oxide,” *Japanese J. Appl. Physics, Part 2 Lett.*, vol. 46, pp. 685–687, 2007.

[40] T. Koida, H. Fujiwara, and M. Kondo, “High-mobility hydrogen-doped In2 O3 transparent conductive oxide for a-Si:H/c-Si heterojunction solar cells,” *Sol. Energy Mater. Sol. Cells*, vol. 93, pp. 851–854, 2009.

[41] T. Koida, H. Sai, and M. Kondo, “In 2O 3:H transparent conductive oxide films with high mobility and near infrared transparency for optoelectronic applications,” *Surf. Eng.*, vol. 28, pp. 102–107, 2012.

[42] Z. Crossbeam, F. Pérez-Willard, and T. M. Friedlmeier, “FIB-SEM Investigations of the Microstructure of CIGS Solar Cells ZEISS Crossbeam FIB-SEM Investigations of the

Microstructure of CIGS Solar Cells," *Appl. Note*, pp. 1–6, 2018.

[43] P. Barquinha, R. Martins, L. Pereira, and E. Fortunato, "N-Type Transparent Semiconducting Oxides," in *Transparent Oxide Electronics*, 9780470683736, vol. 1, pp. 9–61, 2012.

[44] I. Hamberg and C. G. Granqvist, "Evaporated Sn-doped In2O3 films: Basic optical properties and applications to energy-efficient windows," *J. Appl. Phys.*, vol. 60, pp. R122–R159, 1986.

[45] C. G. Granqvist and A. Hultåker, "Transparent and conducting ITO films: New developments and applications," *Thin Solid Films*, vol. 411, pp. 1–5, 2002.

[46] A. N. Tiwari, G. Khrypunov, F. Kurdzesau, D. L. Bätzner, A. Romeo, and H. Zogg, "CdTe solar cell in a novel configuration," *Prog. Photovoltaics Res. Appl.*, vol. 12, pp. 33–38, 2004.

[47] C. Y. Kim and D. H. Riu, "Texture control of fluorine-doped tin oxide thin film," *Thin Solid Films*, vol. 519, pp. 3081–3085, 2011.

[48] K. Subba Ramaiah and V. Sundara Raja, "Structural and electrical properties of fluorine doped tin oxide films prepared by spray-pyrolysis technique," *Appl. Surf. Sci.*, vol. 253, pp. 1451–1458, 2006.

[49] J. Keller *et al.*, "Direct comparison of atomic layer deposition and sputtering of In2O3:H used as transparent conductive oxide layer in CuIn1−xGaxSe2 thin film solar cells," *Sol. Energy Mater. Sol. Cells*, vol. 157, pp. 757–764, 2016.

[50] T. Koida, M. Kondo, K. Tsutsumi, A. Sakaguchi, M. Suzuki, and H. Fujiwara, "Hydrogen-doped In2O3 transparent conducting oxide films prepared by solid-phase crystallization method," *J. Appl. Phys.*, vol. 107, pp. (033514)1-11, 2010.

[51] G. C. E. Jost, A. N. Hamri, F. Köhler, and J. Hüpkes, "Reliability aspects of hydrogen-doped indium oxide," *Phys. Status Solidi Appl. Mater. Sci.*, vol. 213, pp. 1751–1759, 2016.

[52] M. Boccard, N. Rodkey, and Z. C. Holman, "High-mobility Hydrogenated Indium Oxide without Introducing Water during Sputtering," *Energy Procedia*, vol. 92, pp. 297–303, 2016.

[53] Y. Magari, T. Kataoka, W. Yeh, and M. Furuta, "High-mobility hydrogenated polycrystalline In2O3 (In2O3:H) thin-film transistors," *Nat. Commun.*, vol. 13, pp. 1–8, 2022.

[54] D. L. Smith, *Thin-film deposition: principles and practice*, 0-07-058502-4, vol. 33, pp. 476-502, 1996.

[55] J. Kim *et al.*, "Effect of IGZO thin films fabricated by Pulsed-DC and RF sputtering on TFT characteristics," *Mater. Sci. Semicond. Process.*, vol. 120, pp. 105264, 2020.

[56] D. Fuster *et al.*, "System for manufacturing complete Cu(In,Ga)Se2 solar cells in situ under vacuum," *Sol. Energy*, vol. 198, pp. 490–498, 2020.

[57] X. Dai, A. Zhou, L. Feng, Y. Wang, J. Xu, and J. Li, "Molybdenum thin films with low resistivity and superior adhesion deposited by radio-frequency magnetron sputtering at elevated temperature," *Thin Solid Films*, vol. 567, pp. 64–71, 2014.

[58] R. Muydinov *et al.*, "Crystallisation phenomena of In 2 O 3 :H films," *Materials (Basel).*, vol. 12, pp. 1–20, 2019.

[59] M. L. Addonizio, A. Spadoni, A. Antonaia, I. Usatii, and E. Bobeico, "Hydrogen-doped In2O3 for silicon heterojunction solar cells: Identification of a critical threshold for water content and rf sputtering power," *Sol. Energy Mater. Sol. Cells*, vol. 220, pp. 1–12, 2021.

[60] S. Limpijumnong, P. Reunchan, A. Janotti, and C. G. Van De Walle, "Hydrogen doping in indium oxide: An ab initio study," *Phys. Rev. B - Condens. Matter Mater. Phys.*, vol. 80, pp. 1–4, 2009.

[61] T. Koida, H. Fujiwara, and M. Kondo, "Structural and electrical properties of hydrogen-doped In2 O3 films fabricated by solid-phase crystallization," *J. Non. Cryst. Solids*, vol. 354, pp. 2805–2808, 2008.

[62] D. Erfurt, "New TCO for Use as Transparent Front Contact in Chalcopyrite Thin Film Solar Cells," Technischen Universität Berlin zur Erlangung des akademischen Grades, 2019, Doctoral Thesis Dissertation.

[63] R. D. Shannon, "Ionic radii and systematic studies of interatomie distances in halides and chaleogenides central research and development department, experimental," *Acta Cryst.*, vol. A, pp. 751–767, 1976.

[64] N. Nadaud, N. Lequeux, M. Nanot, J. Jové, and T. Roisnel, "Structural studies of tin-doped indium oxide (ITO) and In4Sn3O12," *J. Solid State Chem.*, vol. 135, pp. 140–148, 1998.

[65] J. Rodríguez, M. Gómez, J. Ederth, G. A. Niklasson, and C. G. Granqvist, “Thickness dependence of the optical properties of sputter deposited Ti oxide films,” *Thin Solid Films*, vol. 365, pp. 119–125, 2000.

[66] M. Naftaly *et al.*, “Sheet resistance measurements of conductive thin films: A comparison of techniques,” *Electron.*, vol. 10, pp. 1–10, 2021.

[67] H. F. Wardenga, M. V. Frischbier, M. Morales-Masis, and A. Klein, “In situ hall effect monitoring of vacuum annealing of In2O3:H thin films,” *Materials (Basel).*, vol. 8, pp. 561–574, 2015.

[68] F. Couzinié-Devy, “Re-investigation of preferential orientation of Cu(In,Ga)Se2 thin films grown by the three-stage process,” *Prog. Photovoltaics Res. Appl.*, vol. 20, pp. 527–536, 2011.

[69] M. Marudachalam, R. W. Birkmire, H. Hichri, and E. Al., “Phases , morphology , and diffusion in thin films,” *J. Appl. Phys.*, vol. 82, no. 6, pp. 2896–2905, 1998.

[70] H. Dittrich, U. Prinz, J. Szot, and H. W. Schock, *Proceedings of the 9th European Communities Photovoltaic Solar Energy Conference*, 0-7923-0497-7, vol. 2. 1989.

[71] Y. Hirai, Y. Kurokawa, and A. Yamada, “Numerical study of Cu (In , Ga) Se2 solar cell performance toward 23 % conversion efficiency,” *Japanese J. Appl. Phys.*, vol. 012301, 2013.

[72] K. Medjoubi, “Investigation of the emerging III-V // Si tandem solar cell behavior under irradiations for space applications,” Institut Polytechnique de Paris, 2021, Doctoral Thesis Dissertation.

[73] M. Terheggen, H. Heinrich, G. Kostorz, F. J. Haug, H. Zogg & A. N. Tiwari, “Ga2O3 segregation in Cu(In, Ga)Se2/ZnO superstrate solar cells and its impact on their photovoltaic properties,” *Thin Solid Films*, vol. 403–404, pp. 212–215, 2002.

[74] S. Zahedi-Azad, M. Maiberg, & R. Scheer, “Effect of Na-PDT and KF-PDT on the photovoltaic performance of wide bandgap Cu(In,Ga)Se2 solar cells,” *Progress in Photovoltaics: Research and Applications*, vol. 28, pp. 1146–1157, 2020.

[75] A. Mudryi, V. Gremenok, A. Karotki, V. Zalesski, M. Yakushev, F. Luckert & R. Martin, “Structural and optical properties of thin films of Cu(In,Ga)Se2 semiconductor compounds,” *Journal of Applied Spectroscopy*, vol. *77*, pp. 335–342, 2010.